THE ASTROPHYSICAL JOURNAL, 362:147–164, 1990 October 10

MOLECULAR CLOUDS ASSOCIATED WITH LUMINOUS FAR-INFRARED SOURCES IN THE OUTER GALAXY

JOHN M. CARPENTER, RONALD L. SNELL, AND F. PETER SCHLOERB
Five College Radio Astronomy Observatory, Department of Physics and Astronomy, University of Massachusetts at Amherst
Received 1990 January 11; accepted 1990 April 11

ABSTRACT

The stellar content and physical properties of the molecular clouds associated with 21 bright far-infrared sources in the outer Galaxy have been determined through ^{12}CO, ^{13}CO, 6 cm radio continuum, and *IRAS* observations. The molecular cloud masses range from 200 to $\sim 10^4$ $M_\odot$. The far-infrared luminosity-to-mass ratio for these clouds has a mean value of 6.8 $L_\odot/M_\odot$ and shows no correlation with the cloud mass, a result similar to that found for more massive clouds in the inner Galaxy. The radio continuum survey of the 21 bright far-infrared sources indicates that most of these regions probably have a single, massive star providing most of the ionization. The cloud masses derived from virial and LTE analyses are in agreement, supporting the assumptions commonly made in their calculations, and we find a tight, near-linear correlation between the ^{12}CO luminosity and the cloud mass. The H_2 column density and integrated ^{12}CO intensity are also correlated on a point-by-point basis, although the scatter is larger than the ^{12}CO luminosity–cloud mass relation.

Subject headings: galaxies: The Galaxy — interstellar: molecules — infrared: sources

I. INTRODUCTION

A complete understanding of the present level of star formation activity in the Galaxy requires knowledge of the properties of molecular clouds and the stars that are forming within. The masses, densities, and environments of clouds are just a few of the possible factors that may influence the rate of star formation and the type of stars that have formed. In this study we present an analysis of the stellar content and properties of a sample of molecular clouds associated with 21 bright far-infrared sources in the outer Galaxy. Our observations will be used to determine the relationship between the rate of massive stars forming within these clouds and basic molecular cloud properties.

The estimation of some global cloud properties has been relatively straightforward for some time. Observations of millimeter-wave spectral lines, such as ^{12}CO and ^{13}CO, permit the mass of molecular gas and its distribution to be determined and provide critical information about the kinematics of clouds. However, even though these observations trace the underlying potential for star formation, they alone do not provide a complete picture of a given region, since they do not provide information on the stellar content in molecular clouds.

Observations in the far-infrared by the *Infrared Astronomical Satellite* (*IRAS*) have extended our knowledge of molecular clouds by tracing properties which are complementary to those inferred through molecular line observations. The far-infrared emission from molecular clouds arises from dust grains, and thus contains direct information on the temperature and mass distribution of the dust. Perhaps more important, however, these observations provide an exceptionally useful tracer of the embedded stellar population and the star formation activity, since embedded stars are an important heating source for dust in molecular clouds.

Studies which combine molecular line and far-infrared observations of objects provide crucial information about the nature of star formation that is occurring in molecular clouds. In our own Galaxy, comparisons of *IRAS* observations with the Massachusetts–Stony Brook CO Survey (Sanders *et al.* 1986) have provided information on the star formation within molecular clouds in the inner Galaxy (Mooney and Solomon 1988, hereafter MS; Scoville and Good 1989, hereafter SG). The results of these studies have been interesting in that they have suggested that a few massive molecular clouds with vigorous star formation activity contribute a significant fraction of the total far-infrared luminosity of the inner Galaxy. At the same time, it appears that the rate of star formation per unit mass is independent of the cloud mass.

The studies of inner Galactic clouds are important to our understanding of the origin of the far-infrared emission in our Galaxy and in external galaxies. However, for determining the detailed relationship between far-infrared emission and molecular line emission in an individual cloud, they suffer serious drawbacks. A major problem with the comparison of far-infrared and molecular line observations of the inner Galaxy is the confusion which arises from having many sources along the line of sight. Clouds in this region are often severely blended, making it difficult to discern cloud boundaries and assign far-infrared emission to a particular object. Indeed, in a recent study of a $3° \times 3°$ field in the Massachusetts–Stony Brook CO Survey, Lee, Snell, and Dickman (1990) found that 70% of the ^{12}CO emission is below the 4 K level used by the previous investigators to define the extent of clouds (Solomon *et al.* 1987; Scoville *et al.* 1987). Thus large errors in cloud sizes and masses may arise in this region, and, for observations in the far-infrared, line-of-sight confusion in the far-infrared emission may lead to significant errors in the assessment of a particular cloud's far-infrared luminosity.

In this paper, we have adopted a different approach to the study of star formation within molecular clouds by conducting a survey of active star-forming regions in the outer Galaxy. These objects are far less crowded, and should permit improved estimates of the far-infrared and millimeter properties for the individual objects. We have selected 21 of the brightest far-infrared sources in the *IRAS Point Source Catalog* (1985) in the outer Galaxy for study. Maps were obtained of ^{12}CO, ^{13}CO, and 6 cm radio continuum in addition to the

TABLE 1

OBSERVED SOURCES

IRAS Source (1)	R.A. (1950) (2)	Decl. (1950) (3)	V_{LSR} (km s^{-1}) (4)	Distance (kpc) (5)	Associated Object[a] (6)
00338+6312[b]	00^{h}33^{m}53^s.3	+63°12′32″	−17.7	1.6	RNO 1
00494+5617[b]	00 49 27.8	+56 17 28	−30.4	2.2	Near S184/NGC 281
02575+6017[c,d]	02 57 35.6	+60 17 22	−38.4	2.2	Near IC 1848A
02593+6016[d]	02 59 20.6	+60 16 08	−37.8	2.2	S201
03064+5638	03 06 26.9	+56 38 56	−39.7	2.2	
04324+5106	04 32 28.7	+51 06 39	−35.8	6.0	Near S211
04329+5047	04 32 58.3	+50 47 21	−38.7	6.0	S211
05100+3723	05 10 01.7	+37 23 35	−5.8	2.6	S228
05197+3355	05 19 46.4	+33 55 39	−3.7	3.2	Near S230
05274+3345[b]	05 27 27.6	+33 45 37	−3.7	1.8	Near S237
05375+3540[e]	05 37 32.1	+35 40 45	−17.4	1.8	S235A
05377+3548[e]	05 37 46.7	+35 48 25	−18.7	1.8	Near S235
05490+2658[b]	05 49 05.2	+26 58 52	+0.3	2.1	Near S242
05553+1631[b]	05 55 20.3	+16 31 46	+5.3	2.5	
06056+2131[c,f]	06 05 40.9	+21 31 32	+2.9	1.5	Near S247
06058+2138[c,f]	06 05 53.9	+21 38 57	+4.2	1.5	Near S247
06068+2030	06 06 53.0	+20 30 41	+8.4	1.5	S252E
06073+1249	06 07 23.5	+12 49 24	+25.3	4.8	S270
06117+1350	06 11 46.4	+13 50 33	+17.7	3.8	S269
06155+2319	06 15 32.7	+23 19 26	−6.3	1.6	BFS 51
06308+0402[b]	06 30 52.7	+04 02 27	+15.3	1.6	RNO 73

[a] BFS: Blitz, Fich, and Stark 1982; RNO: Cohen 1980; S: Sharpless 1959.
[b] Outflow reported by Snell, Dickman, and Huang 1990.
[c] Outflow reported by Snell *et al.* 1988.
[d] Millimeter and *IRAS* data for 02575+6017 and 02593+6016 are presented in one map.
[e] Millimeter and *IRAS* data for 05375+3540 and 05377+3548 are presented in one map.
[f] Millimeter and *IRAS* data for 06056+2131 and 06058+2138 are presented in one map.

IRAS co-added fields of these regions, in order to determine the molecular gas content of these clouds and to characterize the star formation occurring within them. The sources represent a subsample of a selection of *IRAS* point sources which are bright ($S_\nu > 500$ Jy at 100 μm) and located in the outer Galaxy ($0^h < \alpha < 12^h$; $\delta > 0°$). In all, a total of 53 sources satisfied the above criteria, and after removal of M82 and IRC +10216 from this list, we arbitrarily selected the 21 sources presented here for this study. Twenty-three of the 51 sources, and 10 of the 21 sources considered here, show evidence of a molecular outflow in their ^{12}CO spectra (Lada 1985; Snell *et al.* 1988; Snell, Dickman, and Huang 1990). The presence of many molecular outflows combined with the observed infrared colors and strong ^{12}CO emission (Snell, Dickman, and Huang 1990) is a strong indication that these infrared sources are young stellar objects which remain embedded in the molecular clouds in which they formed.

The observations of the 21 sources and the data reduction procedures will be described in § II. In § III contour maps of the objects are presented, and a brief discussion of the individual sources is given. The properties of the molecular clouds and the embedded stars associated with the *IRAS* point sources as determined from the spectral line analysis and continuum observations are summarized in § IV. A discussion and analysis of the results and comparison of the derived cloud properties with clouds in the inner Galaxy is presented in § V, followed by a summary of our conclusions in § VI.

II. OBSERVATIONS

The *IRAS* point source name and the right ascension and declination (1950 epoch) for the 21 sources in our sample are given in columns (1)–(3) in Table 1. The radial velocity of the molecular cloud with respect to the local standard of rest (V_{LSR}) and the adopted distances to the objects are given in the subsequent columns. The last column lists the optical identification of the *IRAS* sources or any nearby H II regions. The distances to the *IRAS* sources, discussed by Snell *et al.* (1988) and Snell, Dickman, and Huang (1990), are assigned by their association in position and velocity with well-studied H II regions and OB associations that have distance estimates, often based on optical spectroscopy. Many of the sources lie at a distance between 1.5 and 2.5 kpc and are probably located in the Perseus spiral arm of the Galaxy.

a) Millimeter Observations

Each source listed in Table 1 was mapped in the $J = 1$–0 transitions of ^{12}CO (115.271203 GHz) and ^{13}CO (110.201370 GHz) between 1987 October and 1988 June with a cooled 3 mm Schottky diode mixer receiver on the 14 m telescope of the Five College Radio Astronomy Observatory (FCRAO)[1] in New Salem, Massachusetts. The full width at half-power beam size of the telescope is 45″ at 115 GHz and 47″ at 110 GHz. The observations were made in single-sideband mode with a typical total system noise temperature referred to above the atmosphere of 600 K at 115 GHz and 400 K at 110 GHz. The signal was simultaneously fed into two 256 channel filter banks with spectral resolutions of 250 kHz and 1 MHz, providing velocity resolutions of 0.65 and 2.61 km s^{-1}, respectively, at 115 GHz (0.68 and 2.73 km s^{-1} at 110 GHz). Only the 250 kHz data are presented in this paper.

[1] The FCRAO is operated with support from the National Science Foundation (grant AST 88-15406) and with the permission from the Metropolitan District Commission of the Commonwealth of Massachusetts.

The ^{12}CO and ^{13}CO spectra were obtained at the same positions in the cloud at 1.'0 sampling by position switching against a ^{12}CO emission-free region. The data were corrected for atmospheric attenuation by the standard chopper-wheel technique of observing an ambient temperature load and the sky emission. Telescope and radome losses caused by forward scattering and spillover (η_{fss}) have been determined from previous FCRAO observations of the Moon to be $\sim$0.7. The antenna temperatures corrected for the atmosphere and telescope losses are presented as T_R^*, following the nomenclature suggested by Kutner and Ulich (1981). The ^{12}CO and ^{13}CO data used in the calculations of the cloud masses and luminosities described in the following section have been further corrected for the source coupling coefficient (η_c), which describes the coupling of the beam power pattern with the source size; η_c is estimated to be $\sim$0.7 for the cloud sizes in our sample. Antenna temperatures corrected in this manner are denoted as T_R (see Kutner and Ulich 1981).

b) *IRAS Data Reduction*

Co-added *IRAS* survey data at 12, 25, 60, and 100 μm were obtained for each source. Fields 4° × 4° sampled every 1.'0 were analyzed; the angular resolutions of these images were 0.'5 × 4.'5, 0.'76 × 4.'7, 1.'5 × 4.'7, and 3.'0 × 5.'0, respectively. These images were obtained in order to determine the environment of the sources. The large fields imaged were also helpful in removing the background Galactic and zodiacal emission. Since all the *IRAS* sources in our sample have intensities at 60 and 100 μm which are several orders of magnitude above the fluctuations in the background, the integrated flux density around the *IRAS* sources at these wavelengths is not very sensitive to the specific background removed.

c) *VLA Observations*

Radio continuum observations at 6 cm were made with the Very Large Array (VLA)[2] in D-configuration in 1988 August. The central coordinates of the "snapshots" are given in columns (2) and (3) of Table 1. Each source was observed for approximately 7 minutes in two 50 MHz bands centered at 4835 and 4885 MHz. The primary flux calibrator, observed at the beginning of the run, was 3C 48 with adopted flux densities of 5.63 Jy at 4835 MHz and 5.57 Jy at 4885 MHz. The full width at half-power of the synthesized beam was typically 13″ × 12″ for sources with right ascension $\lesssim 5^h$; the beam shape deteriorated to $\sim$20″ × 12″ thereafter as the elevation of the sources decreased. The primary beam has a full width at half-power of $\sim$9′, and the largest structures visible in our snapshots at 6 cm in D-configuration are approximately 2.'5. The program MX in the AIPS data reduction package was used to clean the images. Uniform weighting of the baselines was used to optimize the resolution, and the images were corrected for primary beam attenuation using the routine PBCOR in AIPS.

III. RESULTS

a) *Maps of the Sources*

Each *IRAS* point source was mapped in ^{12}CO and ^{13}CO out to an extent of $T_R^*(^{12}\mathrm{CO}) \lesssim 2$ K. Our observations of ^{12}CO and ^{13}CO have typical rms noise levels in the 250 kHz filters of $T_R^* \sim 0.35$ and $\sim$0.25 K, respectively. In a few cases the ^{13}CO maps were truncated short of the extent of the ^{12}CO map when it was clear that little emission lay beyond the mapped area. Since the more extended ^{12}CO emission is weak, the bulk of the mass associated with the *IRAS* point source has probably been accounted for. In three cases (02575+6017/02593+6016, 05375+3540/05377+3548, and 06056+2131/06058+2138) two point sources were sufficiently close to be mapped together. The integrated properties (e.g., mass, luminosity, etc.) of these three regions encompass an area including both *IRAS* point sources in the following discussions. Thus our sample consists of 18 molecular clouds containing 21 bright far-infrared sources.

Contour maps for each source are displayed in Figures 1*a*–1*r*; the peak temperature, T_R^*, of the ^{12}CO $J = 1$–0 spectral lines, the integrated ^{13}CO $J = 1$–0 intensity, $\int T_R^* dv$ (K km s^{-1}), and the 100 μm intensity (Jy sr^{-1}) images within the ^{12}CO map boundary are displayed in the left-hand, central, and right-hand panels, respectively, in each figure. Note that the contours of the 100 μm images are logarithmic in order to show the full dynamical range of the emission in these clouds. The center of each map ($\Delta\alpha = 0$, $\Delta\delta = 0$) corresponds to the coordinates in Table 1. The filled squares in the 100 μm images mark the location of peak emission from the radio continuum sources detected at 6 cm with the VLA. The ^{12}CO and ^{13}CO emission peaks are within 1.'0 of the peak 100 μm emission in all 21 sources. Such a close relationship between the millimeter and far-infrared emission strongly suggests that dust associated with the molecular material and heated by newly formed stars is responsible for the brightest far-infrared sources in the outer Galaxy.

b) *Radio Continuum Observations*

Radio continuum observations were made with the VLA at 6 cm to identify the sources of far-infrared emission, presumably massive stars, in these molecular clouds. A summary of the observational data is presented in Table 2. The coordinate offsets of the detected radio continuum sources relative to the *IRAS* point source positions are listed in columns (4) and (5), and the integrated and peak flux densities are given in columns (6) and (7). The angular sizes for each of the radio sources are given in column (8). In most cases they were obtained from Gaussian fits to the cleaned images. Upper limits are given for the unresolved sources, and no size estimates were given for the sources detected near the threshold of our sensitivity. A total of 33 radio continuum sources in the 21 VLA fields have been detected. Sources were detected in the vicinity of all 21 *IRAS* point sources, and in 19 sources a radio continuum peak is within 1.'0 of a far-infrared emission peak listed in the *IRAS Point Source Catalog*.

With the sensitivity of the VLA, some of the radio continuum sources detected near the *IRAS* sources could be background galaxies. From the source counts made by Bennett *et al.* (1983) with the VLA in D-configuration at 6 cm, we would expect to detect $\sim$0.012 background sources arcmin^{-2} above a threshold of 1.0 mJy beam^{-1}, corresponding to a probability of only 5% that one of the sources detected within 1.'0 of the *IRAS* point source position as a background object. Considering the uncertainties in the *IRAS* point source positions, we will assume that the 20 radio sources detected within 1.'0 of the far-infrared sources and the additional sources near 05197+3355, 05375+3540, and 06117+1350 are indeed free-

[2] The VLA is a facility of the National Radio Astronomy Observatory, which is operated by Associated Universities, Inc., under contract with the National Science Foundation.

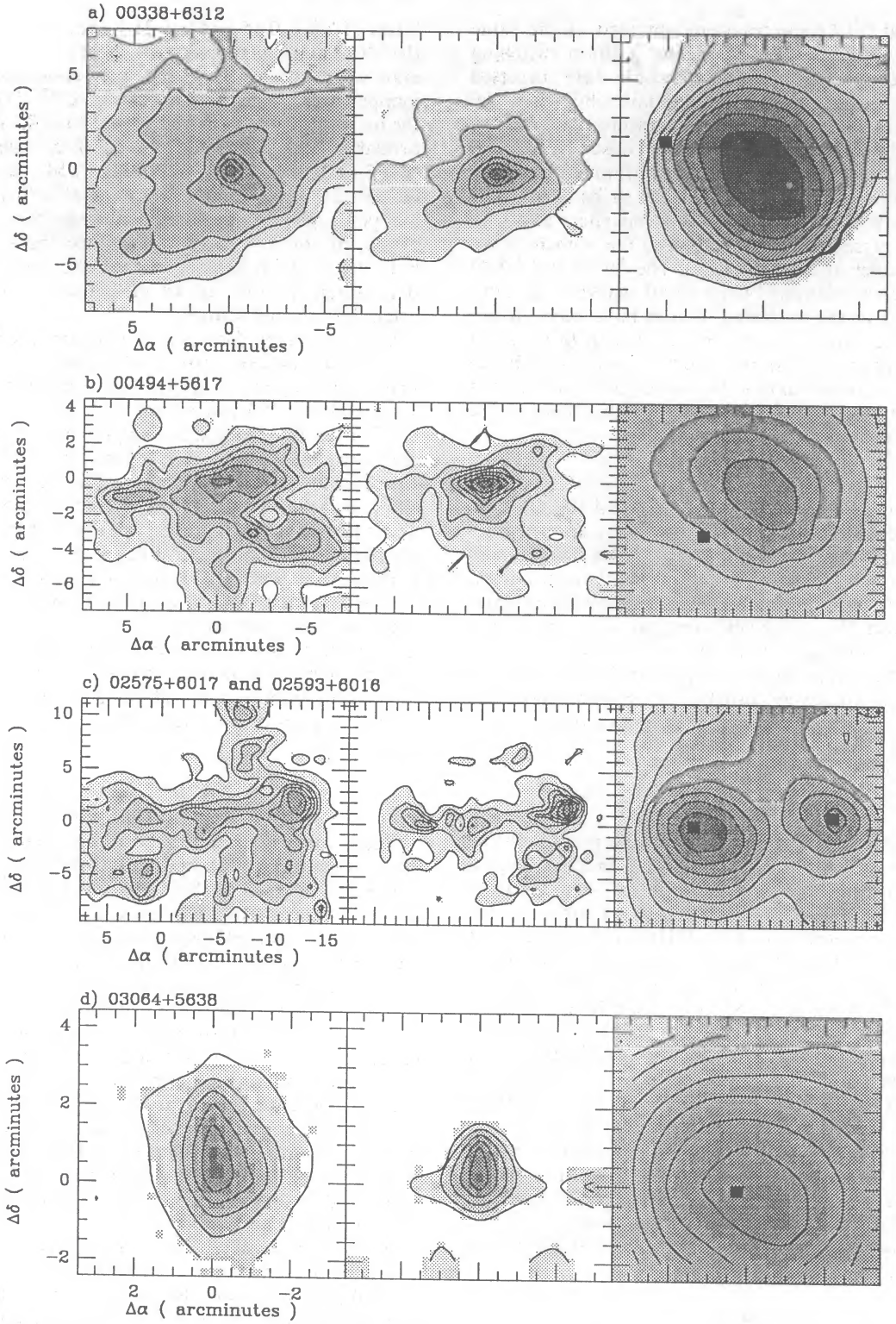

FIG. 1.—(*a*) *Left panel*: Contour map of peak ^{12}CO $J = 1$–0 antenna temperature (T_R^*). Contours start at 1.5 K, with steps of 2.0 K. Coordinate offsets are with respect to the positions listed in Table 1. *Center panel*: Contour map of the integrated ^{13}CO $J = 1$–0 intensity [$\int T_R^*(^{13}\mathrm{CO})dv$]. Lowest level is 1.5 K km s^{-1}, with steps of 3.0 K km s^{-1}. No ^{13}CO data were taken below $\Delta\delta = -4'.0$ and above $\Delta\alpha = 4'.0$. *Right panel*: Map of the 100 μm intensity from *IRAS*. The contours are logarithmic, with the lowest being 6.2 ($= 1.6 \times 10^6$ Jy sr^{-1}), with logarithmic steps of 0.3. The filled square marks the position of the detected radio continuum source. (*b*) Same as (*a*), except with ^{12}CO contours of 1.5 K and steps of 3.0 K; $\int T_R^*(^{13}\mathrm{CO})dv$ levels of 1.5 K km s^{-1} and steps of 3.0 K km s^{-1}; log 100 μm intensity levels of 7.4 with steps of 0.2. No ^{13}CO data were taken below $\Delta\delta = -6'$ and to the left of $\Delta\alpha = 6'$. (*c*) See (*a*). ^{12}CO: 1.5 K with steps of 3.0 K; ^{13}CO: 1.5 K km s^{-1} with steps of 3.0 K km s^{-1}; log 100 μm intensity: 7.6 with steps of 0.2. The source at ($\Delta\alpha = 0$, $\Delta\delta = 0$) is 02593+6016. No ^{12}CO data were taken in the regions ($\Delta\alpha < 1'$, $\Delta\delta > 5'$) and ($\Delta\alpha < 0'$, $\Delta\delta < -7'$). No ^{13}CO data were taken in the regions $\Delta\delta > 7'$, $\Delta\delta < -7'$, $\Delta\alpha < 4'$, and ($\Delta\alpha < 1'$, $\Delta\delta < -4'$). (*d*) See (*a*). ^{12}CO: 1.5 K with steps of 2.0 K; ^{13}CO: 1.25 K km s^{-1} with steps of 1.0 K km s^{-1}; log 100 μm intensity: 7.9 with steps of 0.1.

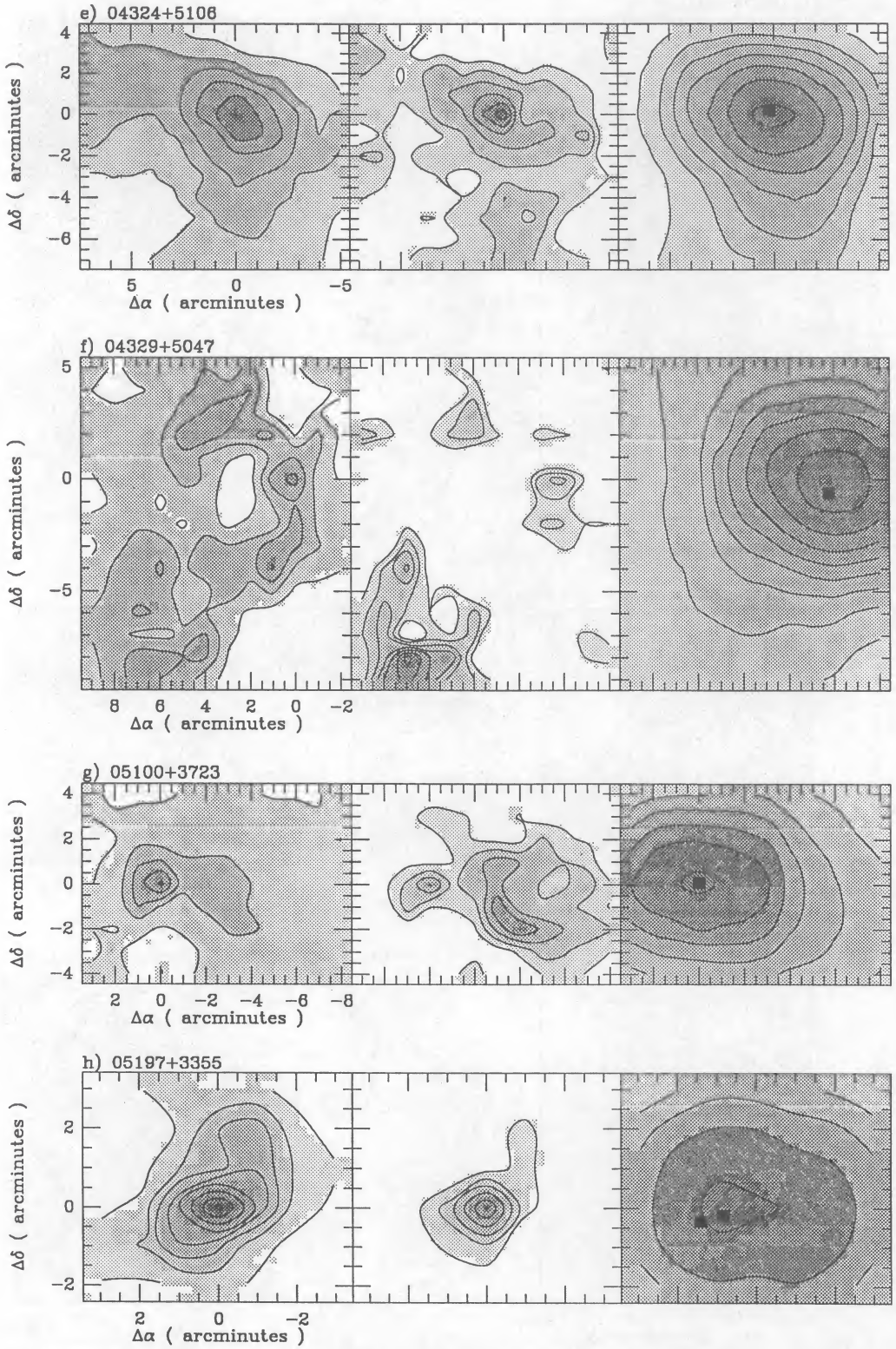

FIG. 1.—(*e*) See (*a*). ^{12}CO: 1.5 K with steps of 2.0 K; ^{13}CO: 1.5 K km s^{-1} with steps of 2.0 K km s^{-1}; log 100 μm intensity: 7.4 with steps of 0.2. (*f*) See (*a*). ^{12}C
1.5 K with steps of 2.0 K; ^{13}CO: 1.5 K km s^{-1} with steps of 1.0 K km s^{-1}; log 100 μm intensity: 7.0 steps of 0.2. (*g*) See (*a*). ^{12}CO: 1.5 K with steps of 3.0 K; ^{13}C
1.5 K km s^{-1} with steps of 2.0 K km s^{-1}; log 100 μm intensity: 7.3 with steps of 0.2. (*h*) See (*a*). ^{12}CO: 1.5 K with steps of 3.0 K; ^{13}CO: 2.0 K km s^{-1} with steps
2.0 K km s^{-1}; log 100 μm intensity: 7.75 with steps of 0.2.

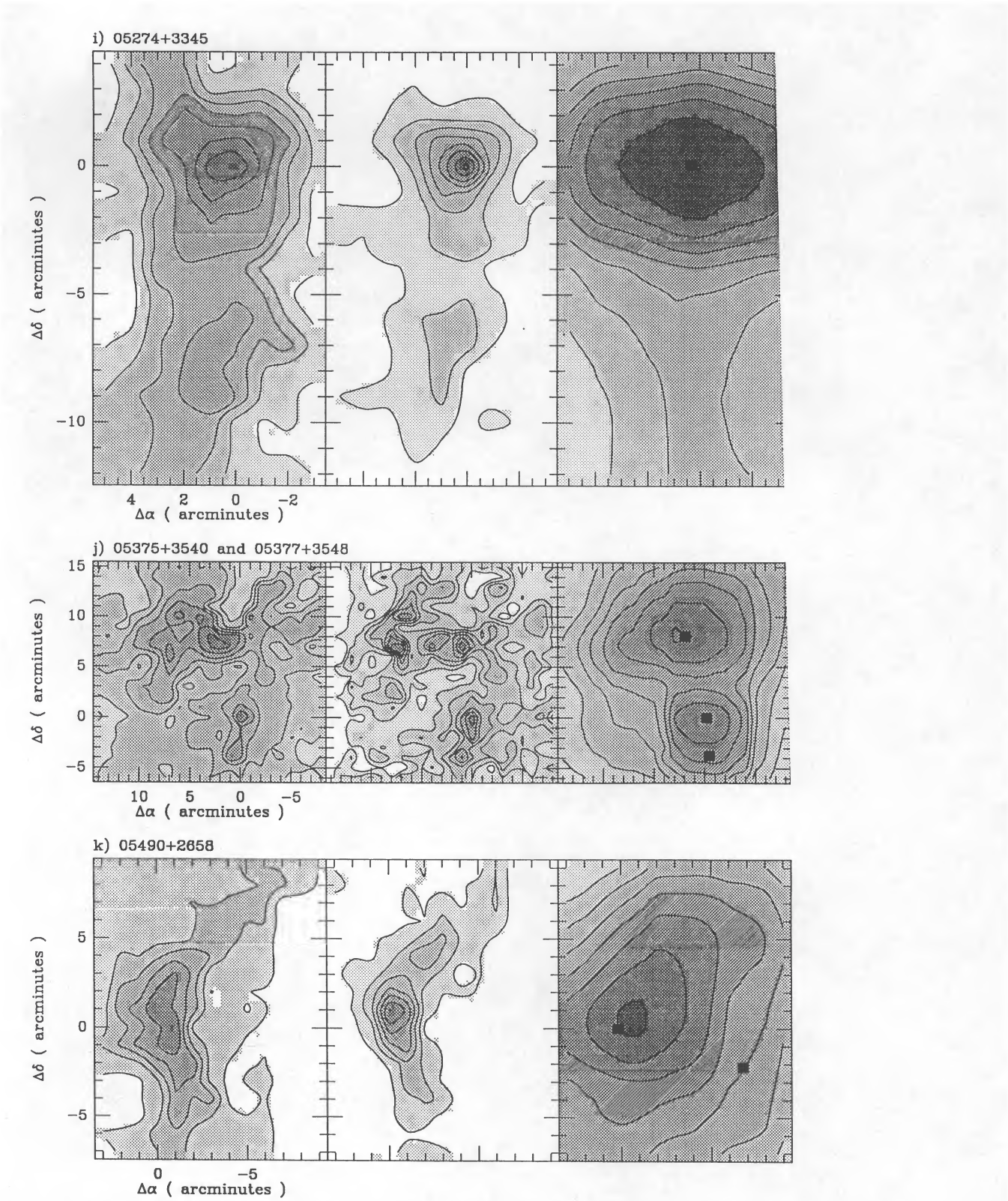

FIG. 1.—(*i*) See (*a*). ^{12}CO: 1.5 K with steps of 2.0 K: ^{13}CO: 1.5 K km s^{-1} with steps of 4.0 K km s^{-1}; log 100 μm intensity: 6.3 with steps of 0.3. No ^{13}CO data were taken below $\Delta\delta = -11'$. (*j*) See (*a*). ^{12}CO: 1.5 K with steps of 4.0 K; ^{13}CO: 1.5 K km s^{-1} with steps of 4.0 K km s^{-1}; log 100 μm intensity: 7.6 with steps of 0.2. The source at ($\Delta\alpha = 0$, $\Delta\delta = 0$) is 05375+3540. No ^{13}CO data were taken to the left of $\Delta\alpha = 13'$. (*k*) See (*a*). ^{12}CO: 1.5 K with steps of 3.0 K; ^{13}CO: 2.0 K km s^{-1} with steps of 4.0 K km s^{-1}; log 100 μm intensity: 7.3 with steps of 0.2. No ^{12}CO data were taken in the region ($\Delta\alpha > -6$, $\Delta\delta < 8'$), and no ^{13}CO data were taken to the right of $\Delta\alpha = -6'$.

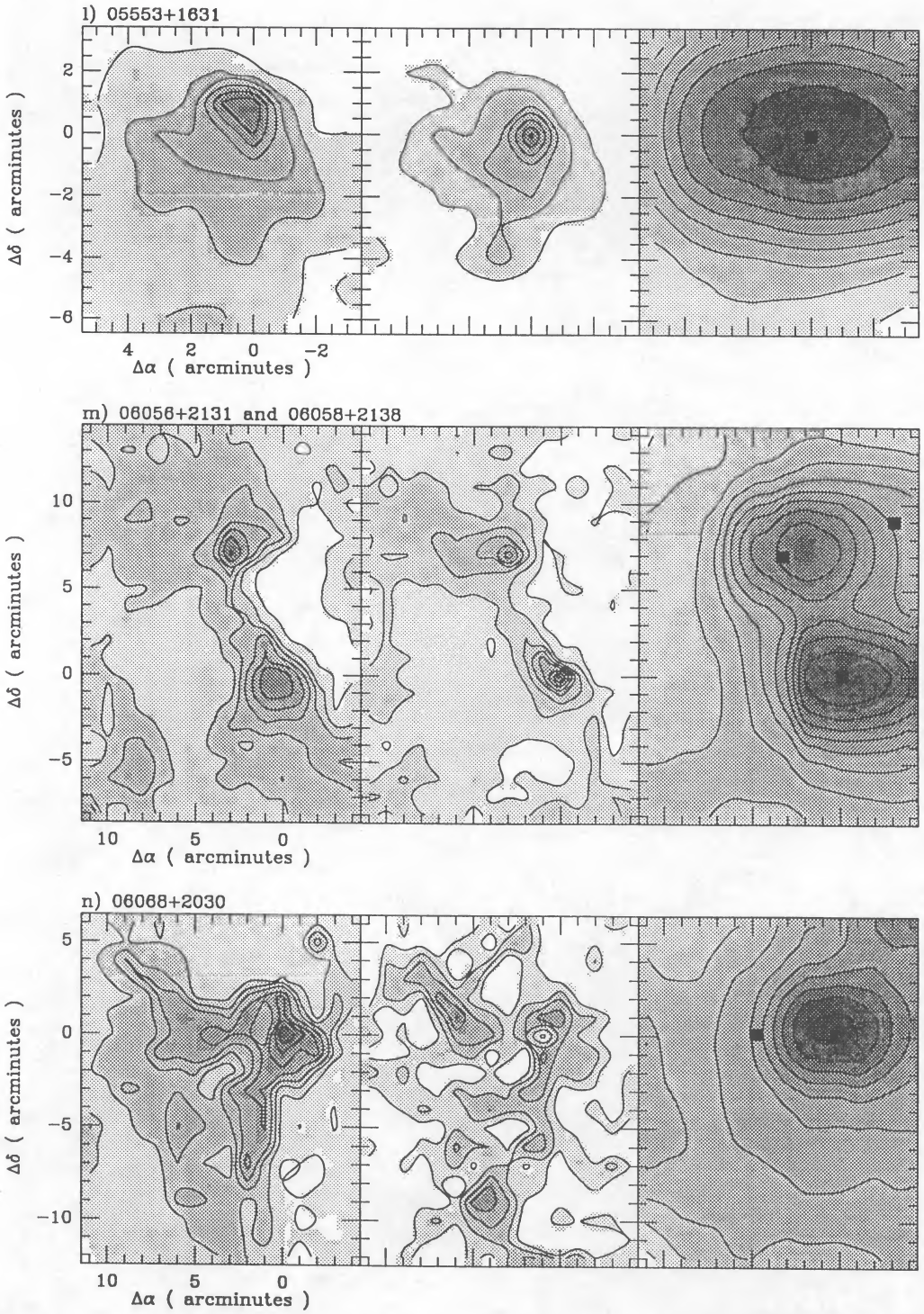

FIG. 1.—(*l*) See (*a*). ^{12}CO: 2.0 K with steps of 3.0 K; ^{13}CO: 1.5 K km s^{-1} with steps of 3.0 K km s^{-1}; log 100 μm intensity: 6.9 with steps of 0.2. No ^{13}CO data were taken below $\Delta\delta = -4'$ and to the right of $\Delta\alpha = -2'$. (*m*) See (*a*). ^{12}CO: 2.0 K with steps of 3.0 K; ^{13}CO: 2.0 K km s^{-1} with steps of 5.0 K km s^{-1}; log 100 μm intensity: 7.2 with steps of 0.2. The source at ($\Delta\alpha = 0$, $\Delta\delta = 0$) is 06056+2131. (*n*) See (*a*). ^{12}CO: 1.5 K with steps of 3.0 K; ^{13}CO: 2.0 K km s^{-1} with steps of 2.0 K km s^{-1}; log 100 μm intensity: 8.0 with steps of 0.1.

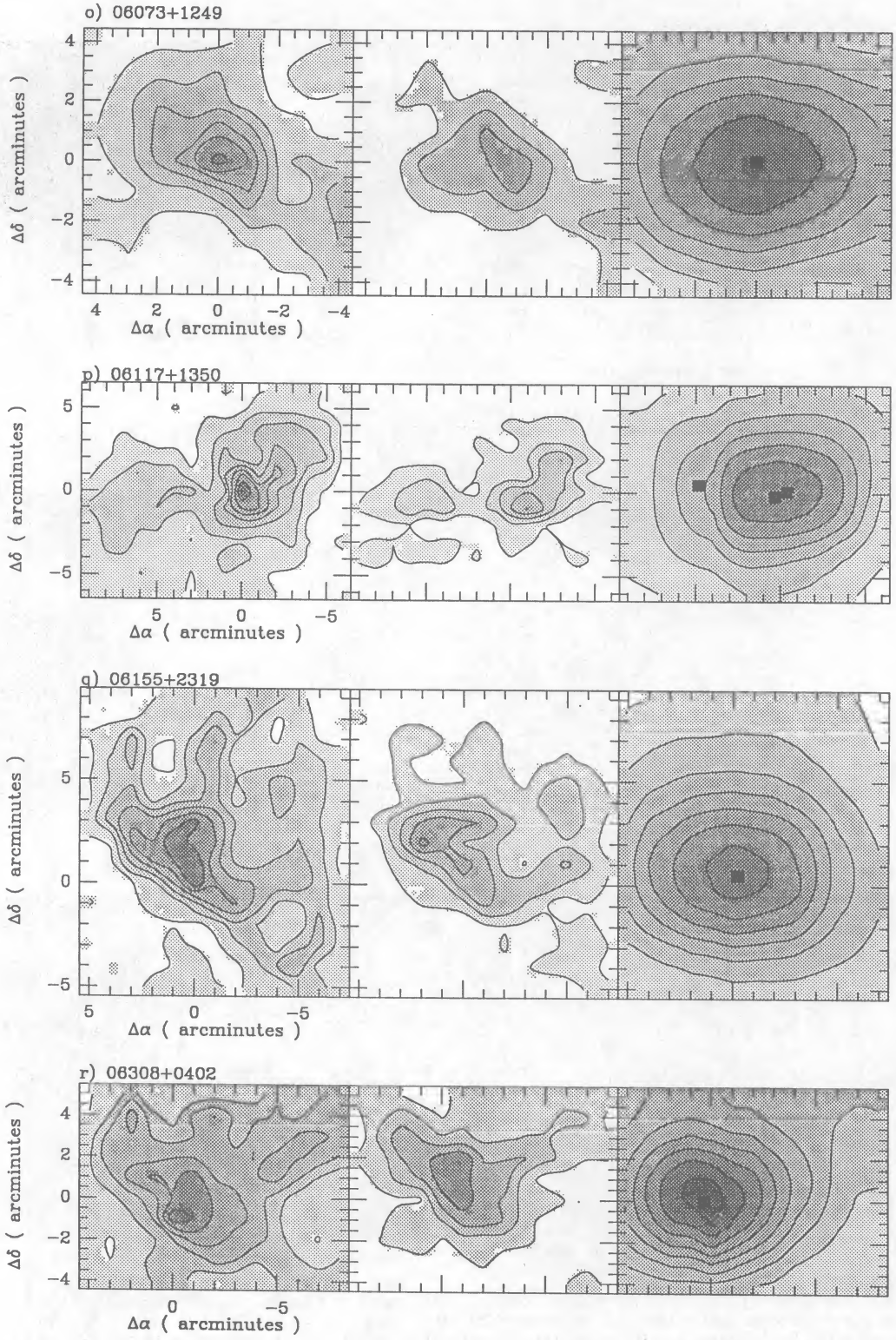

FIG. 1.—(*o*) See (*a*). ^{12}CO: 1.5 K with steps of 3.0 K; ^{13}CO: 1.0 K km s^{-1} with steps of 1.0 K km s^{-1}; log 100 μm intensity: 7.3 with steps of 0.2. (*p*) See (*a*). ^{12}CO: 1.5 K with steps of 3.0 K; ^{13}CO: 1.5 K km s^{-1} with steps of 3.0 K km s^{-1}; log 100 μm intensity: 7.3 with steps of 0.3. No ^{13}CO data were taken below $\Delta\delta = -4'$ and above $\Delta\delta = 4'$. (*q*) See (*a*). ^{12}CO: 1.5 K with steps of 3.0 K; ^{13}CO: 1.25 K km s^{-1} with steps of 2.0 K km s^{-1}; log 100 μm intensity: 7.6 with steps of 0.2. (*r*) See (*a*). ^{12}CO: 1.5 K with steps of 3.0 K; ^{13}CO: 1.0 K km s^{-1} with steps of 2.0 K km s^{-1}; log 100 μm intensity: 8.0 with steps of 0.1.

TABLE 2

SUMMARY OF VLA OBSERVATIONS

IRAS Source (1)	Radio Continuum Peak R.A. (1950) (2)	Decl. (1950) (3)	Offset[a] $\Delta\alpha$ (4)	$\Delta\delta$ (5)	Integrated Flux Density (mJy) (6)	Peak Flux Density (mJy beam^{-1}) (7)	Angular Size (arcsec) (8)
00338+6312	$00^h33^m53^s3$	+63°12′32″	...	...	...	<0.9[b]	...
	00 34 38.1	+63 14 15	5.05	1.72	3.7	3.7 ± 0.9	<10
00494+5617	00 49 27.8	+56 17 28	...	...	...	<1.2[b]	...
	00 49 47.0	+56 14 33	2.66	−2.92	34.4	34.4 ± 0.6	<7
02575+6017	02 57 37.4	+60 17 24	0.22	0.03	3.2	3.2 ± 0.3	<7
02593+6016	02 59 21.9	+60 16 13	0.16	0.08	473	39.7 ± 0.7	43 × 39
03064+5638	03 06 28.7	+56 38 51	0.25	−0.08	84.8	6.7 ± 0.3	48 × 34
04324+5106	04 32 30.1	+51 06 48	0.22	0.15	196	133 ± 0.3	9 × 9
	04 31 32.9	+51 08 14	−8.76	1.58	103	103 ± 10	<11
04329+5047[c]	04 32 59.9	+50 46 45	0.25	−0.60	514	21.9 ± 0.4	82 × 69
05100+3723	05 10 01.7	+37 23 40	0.00	0.08	472	28.1 ± 0.2	56 × 51
05197+3355	05 19 50.4	+33 55 29	0.83	−0.17	18.7	8.1 ± 0.3	19 × 77
	05 19 53.2	+33 55 19	1.41	−0.33	12.9	12.9 ± 0.3	<8
	05 19 43.6	+33 51 14	−0.58	−4.42	15.8	15.8 ± 0.5	<12
	05 19 23.1	+33 51 34	−4.83	−4.09	16.6	16.6 ± 1.2	<7
05274+3345	05 27 29.2	+33 45 42	0.33	0.08	1.0	1.0 ± 0.3	...
05375+3540	05 37 31.1	+35 40 45	−0.20	0.00	248	73.2 ± 0.4	19 × 16
	05 37 30.0	+35 36 59	−0.43	−3.77	54.9	13.1 ± 0.5	22 × 21
05377+3548	05 37 46.3	+35 48 30	−0.08	0.08	5.7	2.3 ± 0.5	22 × 16
05490+2658	05 49 05.9	+26 58 52	0.16	0.00	1.5	1.5 ± 0.3	...
	05 48 34.9	+26 56 42	−6.75	−2.17	27.0	13.9 ± 1.5	13 × 12
05553+1631	05 55 20.3	+16 31 46	0.00	0.00	1.8	1.3 ± 0.3	11 × 7
06056+2131	06 05 40.5	+21 31 37	−0.09	0.08	1.6	1.6 ± 0.4	...
06058+2138	06 05 55.0	+21 38 32	0.26	−0.42	2.0	1.2 ± 0.5	8 × 5
	06 05 27.7	+21 40 32	−6.09	1.58	33.0	28.5 ± 1.9	18 × 13
06068+2030	06 06 53.7	+20 30 46	0.16	0.08	152	21.0 ± 0.3	43 × 38
	06 07 13.3	+20 30 51	4.75	0.17	6.8	6.8 ± 0.5	<15
	06 06 25.2	+20 35 26	−6.51	4.75	84.9	39.1 ± 3.9	22 × 18
06073+1249	06 07 23.5	+12 49 29	0.00	0.08	30.4	23.2 ± 0.3	8 × 7
	06 07 41.3	+12 46 09	4.34	−3.25	7.2	7.2 ± 0.8	<11
06117+1350	06 11 47.8	+13 50 23	0.34	−0.17	613	41.9 ± 0.4	68 × 60
	06 11 44.7	+13 50 38	−0.41	0.08	>19.8[d]	19.8 ± 0.4	...
	06 12 06.3	+13 51 03	4.83	0.50	24.1	7.3 ± 1.3	30 × 20
06155+2319	06 15 31.6	+23 19 56	−0.25	0.50	24.7	2.5 ± 0.3	51 × 41
06308+0402	06 30 54.0	+04 02 27	0.33	0.00	92.2	25.0 ± 0.3	26 × 25

[a] Offset of the peak radio continuum emission position relative to the *IRAS* point source coordinates listed in Table 1.

[b] No radio continuum source was detected at the *IRAS* point source position. The tabulated peak flux density is a 3 σ upper limit.

[c] The coordinates refer to the center of the radio continuum source and not the position of peak emission. See Fig. 2.

[d] Radio continuum emission is blended with the stronger source listed above.

free emission from compact H II regions associated with young stellar objects embedded within the molecular clouds; the second sources listed under 05490+2658 and 06058+2138 may be associated with larger H II regions near the *IRAS* sources (see discussion below).

The other eight radio continuum sources we detected remain unidentified. They do not correspond to any obvious features on the Palomar Observatory Sky Survey (POSS) prints or the *IRAS* survey fields. Those sources within our mapped region are not coincident with a ^{12}CO emission peak. Thus we will assume that these sources are background objects and are not associated with the molecular cloud. The source counts from Bennett *et al.* (1983) suggest that we should have detected a total of ~15 background objects within the 9′ primary beam in the 21 images, roughly consistent with our observations.

c) *Description of the Individual Sources*

As we indicated in Table 1, many of our *IRAS* sources appear to be associated with H II regions. To clarify the spatial relationship between the molecular clouds and radio continuum sources with presumably related objects, we briefly describe each region.

i) *00338+6312*

The *IRAS* source 00338+6312 appears toward a dark obscuring lane on the POSS prints. The source has been associated with Cas OB 14 (Snell, Dickman, and Huang 1990) and is coincident with RNO 1 (Cohen 1980). No radio continuum emission was detected within 5′ of the far-infrared source, and the lack of enhanced molecular or far-infrared emission at the position of the one radio source that was detected toward this region makes it unlikely that this 6 cm continuum source is associated with the molecular cloud.

ii) *00494+5617*

The molecular cloud associated with this source is at the southern edge of the H II region S184. Elmegreen and Lada (1978) have studied this region extensively and found the molecular cloud to be divided into two fragments by a channel of ionized gas. Our maps correspond to the western fragment of the cloud. Elmegreen and Lada (1978) have proposed that

the expansion of S184 has triggered gravitational instabilities along the ionization front–molecular cloud interface and induced star formation (see Elmegreen and Lada 1977). The sharp edge to the ^{12}CO emission at the northern boundary of the cloud that can be seen in Figure 1*b* is along this interface.

Israël (1977) has imaged this region at 21 cm with the Westerbork Array and reports the presence of two extended ($\sim 2'$ diameter) H II regions, one at the *IRAS* point source position and another $\sim 5'$ to the east; the extended nature of these sources probably explains why they escaped detection in our survey. Israël also detected the compact radio source listed in Table 2; he found it to be at the edge of the diffuse H II region and speculates that the source is a compact H II region. The observed flux densities at 6 and 21 cm, though, are not consistent with a thermal source (cf. Table 2 and Israël 1977). Furthermore, the ^{12}CO and far-infrared emission do not peak at this position, so we will assume that it is more likely a background radio source and not associated with the molecular cloud.

iii) *02575+6017 and 02593+6016*

Both sources are located on the eastern side of the nebula IC 1848 (also named W5); 02575+6017 is on the bright rim IC 1848A (following the notation of Pottasch 1956), while 02593+6016 is coincident with S201. The effects of the eastern expansion of the H II region IC 1848 can be seen in Figure 1*c* as a compression of the molecular emission on the right-hand side of the ^{12}CO and ^{13}CO maps. Loren and Wootten (1978) and Thronson *et al.* (1980) have suggested that this may be another example of propagating star formation. They could not, however, rule out the possibility that these exciting stars and the expanding H II region formed independently.

The H II region S201 coincides with 02593+6016 and appears on the POSS plate as a nebula with an obscuring lane running through it. This obscuring material can be seen as an east-west elongation of the ^{12}CO emission in Figure 1*c* (see also Fig. 3*a* in Felli, Hjellming, and Cesaroni 1987). The radio continuum image (see Fig. 1 in Felli, Hjellming, and Cesaroni 1987) shows a fan-shaped H II region that appears density-bounded on the east side. Mampaso *et al.* (1989) have detected five near-infrared sources within $\sim 1\farcm5$ of the *IRAS* point source position.

iv) *03064+5638*

We have mapped the entire extent of the molecular cloud associated with this source above the noise in the ^{12}CO and ^{13}CO data. No optical counterparts to this source appear on the POSS prints.

v) *04324+5106*

Located $\sim 0\farcm5$ north of S211, this infrared source corresponds to a small, faint nebulous region on the POSS charts. We note that Cohen, Jones, and Walker (1989) have assigned a weak ^{12}CO feature at $V_{LSR} = -7$ km s^{-1} to the source 04324+5106, while we find a strong emission line at $V_{LSR} = -37$ km s^{-1}. The coincidence of the peaks of the molecular emission at -37 km s^{-1} and the far-infrared emission supports our identification of the -37 km s^{-1} component with 04324+5106.

vi) *04329+5047*

This source probably belongs to the same molecular cloud complex as 04324+5106. The *IRAS* point source is located near the optical center of S211. The cleaned 6 cm VLA image, presented in Figure 2, shows a ring structure to this H II region.

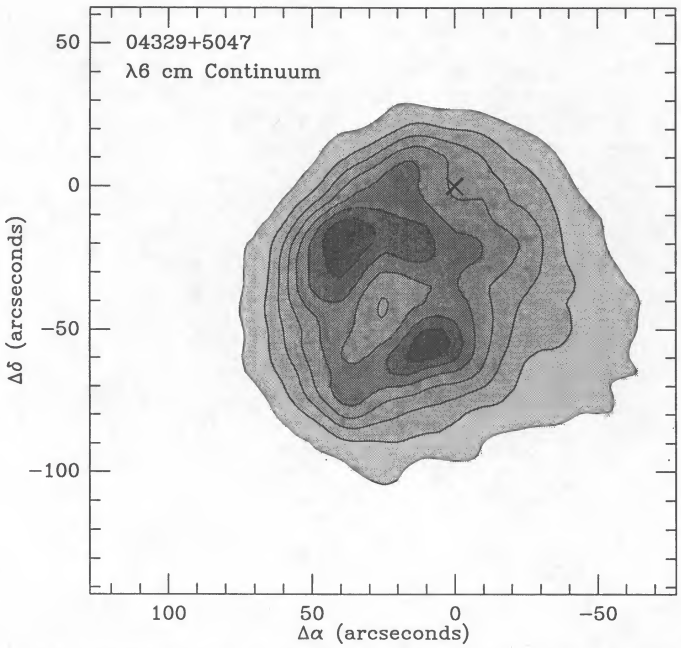

FIG. 2.—Contour map of the 6 cm radio continuum image toward 04329+5047. The cross marks the position of the *IRAS* source. The lowest contour level is 1.2 mJy beam^{-1}, with succeeding levels at steps of 3.0 mJy beam^{-1}.

(The coordinates listed in Table 2 for this source correspond to the center of the radio continuum source and not the position of peak emission.) A 20 cm VLA image taken by Albert *et al.* (1986) at a comparable resolution to our image of S211 does not show this structure.

vii) *05100+3723*

This far-infrared source is coincident with the H II region S228. The molecular cloud associated with 05100+3723 was mapped in ^{12}CO by Lucas and Encrenaz (1975), while Israël (1977) and Albert *et al.* (1986) have observed this source in the radio continuum at 6 and 20 cm, respectively. The radio continuum and *IRAS* source positions are located near the near-infrared source detected by Frogel and Persson (1973). The fan-shaped appearance of the radio continuum image suggests that the ionization front is density-bounded to the north.

viii) *05197+3355*

This *IRAS* source corresponds to a small ($\sim 1'$ in diameter) nebulosity located on the northern edge of S230. Two radio continuum sources were detected within $\sim 1\farcm5$ of the *IRAS* point source position, and both are assumed to be associated with young stellar objects embedded within the molecular cloud.

ix) *05274+3345*

This source is located $\sim 30'$ north of S237 and 1° east of S230. A small, faint H II region is visible on the POSS plates, coincident with the radio continuum and *IRAS* sources.

x) *05375+3540 and 05377+3548*

The far-infrared source 05375+3540 is $\sim 9'$ south of S235 and is coincident with S235A (notation from Israel and Felli 1978). This source appears as a compact emission knot on the POSS plates, which was detected in our radio continuum survey. About $1'$ south of S235A is another compact nebu-

losity, S235B, that was not detected in our VLA survey at 6 cm or in the survey by Israel and Felli at 6 and 21 cm. About 3′ south of S235A is a radio continuum source (S235C; see Table 2) that has no optical counterparts on the POSS plates. Since the radio continuum spectra of S235C is consistent with a thermal source (Israel and Felli 1978) and it is within 1′ of a ^{12}CO emission peak, we will assume that the source is indeed associated with the molecular cloud. We also note that Evans and Blair (1981) have detected a near-infrared source toward S235A and S235B but not toward S235C. The other bright far-infrared source in the region, 05377+3548, lies ~1.5 southeast of the H II region S235 and is coincident with a near-infrared source (Evans and Blair 1981). The molecular cloud encompassing the two *IRAS* sources has been only partially mapped and shows a fragmentary structure at the resolution of our 45″ beam.

xi) *05490+2658*

The *IRAS* source 05490+2658 is located on the eastern edge of the H II region S242. Figure 1*k* clearly shows a curvature in the cloud where the ionization front from S242 has eroded the molecular material. The other radio continuum source detected in our survey lies toward the H II region S242. The CO maps indicate that this H II region has destroyed most of the gas and dust along the line of sight toward this radio continuum source, so that if this source is indeed associated with the S242 nebula, it is unlikely to contribute a significant fraction of the observed far-infrared luminosity in this region. Therefore we will not include this second radio continuum source in the following analyses.

xii) *05553+1631*

This source lies south of a small nebulous region on the POSS prints which appears brighter on the blue plate than on the red, suggesting that the optical object is a reflection nebula. In Figure 1*l* a sharp cutoff in the molecular emission at the northwest boundary between the nebula and the cloud is seen. It is not clear whether the star responsible for the far-infrared emission is also the source producing the reflection nebula.

xiii) *06056+2131 and 06058+2138*

These two sources are located ~3′ east of S247. Figure 1*m* shows that the sources are bordered by the ionization front from S247 to the east, suggestive of the sequential star formation process proposed by Elmegreen and Lada (1977). Kömpe *et al.* (1989) have found the S247 region to be connected to S252 (see below) by a narrow bridge of gas. The second radio source listed in Table 2 under 06058+2138 lies within the S247 nebulosity and is presumably radio emission from the optical H II region. By arguments analogous to those presented in § III*c*(xi), this source will not be included in the following discussions.

xiv) *06068+2030*

This source corresponds to a bright Hα knot within S252 on the POSS prints, located ~3′ east of the main exciting star for the entire region (Garnier and Lortet-Zuckermann 1971). Felli, Habing, and Israël (1977) imaged S252 in the radio continuum at 6 and 21 cm and found six radio continuum emission peaks. In their notation 06068+2030 corresponds to S252E.

Garnier and Lortet-Zuckermann (1971) found an optically visible star (S252a) in S252E and suggest that this star is responsible for the excitation in this emission knot. They estimate a spectral type between O9 and B0 for the star, compared with the B1 V estimate by Grasdalen and Carrasco (1975). The latter spectral type is roughly consistent with the radio continuum emission we observed at 6 cm (see § IV). Grasdalen and Carrasco have attributed the S252E nebulosity to neutral gas reflecting the starlight from S252a. The correspondence of the near-infrared source (Zeilik 1976) and the optical star with the molecular, radio continuum, and far-infrared emission peaks suggests that the star is not entirely free of the molecular cloud.

Lada and Wooden (1979) have mapped S252 in ^{12}CO and found two cloud fragments with our maps corresponding to the eastern cloud fragment. Chavarría-K., de Lara, and Hasse (1987) and Chavarría-K. *et al.* (1989) have reported extensive near-infrared observations of S252, including the detection of a cluster of ~20 stars in S252E.

xv) *06073+1249*

This *IRAS* source is coincident with the H II region S270 on the POSS charts, and was classified as a bipolar nebula by Neckel and Staude (1984). No structure is present in our 6 cm radio continuum image of this H II region.

xvi) *06117+1350*

Chopinet, Deharveng-Baudel, and Lortet-Zuckermann (1974) found this H II region (S269) to be divided in two by a dark band in their Hβ photograph. The *IRAS* source is located at the southern edge of the western lobe. At the far-infrared source position we detected two radio continuum peaks that are slightly blended together. Turner and Terzian (1985) imaged the nebula at 18 cm and resolved a third peak in this region. Heydari-Malayeri *et al.* (1982) has proposed that the B0.5 V star (Moffat, FitzGerald, and Jackson 1979) in the center of the nebula is the main exciting star for the region. As pointed out by Cox, Deharveng, and Caplan (1987), this cannot explain the observed radio continuum flux and suggests the presence of additional stellar sources (see § V). The detection of a near-infrared source (Wynn-Williams, Becklin, and Neugebauer 1974; Persi *et al.* 1987), OH emission (Turner 1971), a H_2O maser (Lo and Burke 1973), and an *IRAS* point source near the radio continuum peaks supports this conclusion. The third source listed in Table 2 under 06117+1350 is located a few arcminutes east of the optical nebulosity. A secondary peak in the ^{12}CO emission is found at this position, and the 100 μm intensity does extend slightly in this direction (see Fig. 1*p*). We will assume, then, that this radio continuum source is also associated with a young stellar object within the molecular cloud.

xvii) *06155+2319*

On the POSS prints, 06155+2319 appears toward an obscuring lane bordering the H II region BFS 51. A sharp cutoff in the molecular emission in the lower left-hand portion of the map in Figure 1*q* corresponds to this border. The optical appearance of this nebula probably resulted from an ionization front bursting through the edge of the molecular cloud.

xviii) *06308+0402*

Cataloged as RNO 73 by Cohen (1980), this source is located 1° south of the Rosette Nebula. Cohen found a cluster of four visible, reddish stars within the 06308+0402 nebulosity.

d) Summary

While all of the objects we have described are bright in the far-infrared, their associated molecular clouds do not seem to possess any extraordinary characteristics. Many of the clouds have angular sizes of only a few arcminutes and have a single

molecular emission peak. However, several of the molecular clouds appear to have been altered by the expansion of a nearby H II region, presumably produced by massive stars outside our mapped regions. Furthermore, some of the radio continuum sources we have detected appeared to have formed on the interface between this expanding H II region and the molecular cloud, reminiscent of the ionization front–induced star formation mechanism proposed by Elmegreen and Lada (1977). The sources 06056+2131/06058+2138 provide extremely tantalizing evidence for this conjecture, since *both* objects are embedded in a molecular cloud on the boundary of the S247 ionization front. However, it is difficult to determine whether the ionization front actually induced star formation or whether the embedded stars formed independently. An interesting follow-up study would be to make a high-resolution map in ^{12}CO of S247 to determine fully the effect of the expanding H II region on the surrounding molecular material.

Finally, since our VLA survey was sensitive to continuum emission on size scales of less than $\sim 2\farcm5$, a diffuse, extended H II region encompassing the compact sources could go undetected; in this situation the emission we have observed would be a lower limit to the actual total flux density. Also, the flux from nearby H II regions could provide a significant contribution to the ionization in the molecular clouds and go undetected in our observations. As examples, Kazés, Le Squéren, and Gadéa (1975) observed a flux density toward 02593+6016 that was a factor of 2.4 greater than our measurement when scanning the source using a single aperture with a $1\farcm5 \times 7'$ beam size, and Gebel (1968) has observed a total flux density of 30 Jy within a $6\farcm4$ beam toward the H II region S252; we measured a flux density of 0.15 Jy for 06068+2030, one of several components in S252. Inspection of Table 2 indicates, though, that many of the sources we have detected are on size scales of 20″ or less, so it is possible that for these compact sources we have indeed observed the total flux. Regardless, the main goal of the VLA observations is to obtain a census of the ionizing stars and accurate positions relative to the *IRAS* point sources and the molecular emission peaks. While we may have missed some of the flux from the ionizing stars, our observations do allow for a first-order analysis of the massive stellar population in these regions.

IV. GLOBAL CLOUD PROPERTIES AND STELLAR CONTENT

In § III we discussed the morphology of a few of the *IRAS* sources based on the observed millimeter, far-infrared, and radio continuum emission. The same data can be used further to deduce quantitatively the global properties of these regions. In §§ IV*a* and IV*b* we will outline our calculations of the molecular cloud masses and discuss the relationship between the cloud mass and the ^{12}CO luminosity. We will then estimate the total luminosity of the embedded stars from the *IRAS* observations in § IV*c* and the spectral type of the individual stars in § IV*d*.

a) Molecular Cloud Masses

Cloud masses are usually estimated by one of two semi-independent means. In one method the masses are calculated from the virial theorem assuming the clouds are gravitationally bound and dynamically relaxed. Considering gravitational forces only, a spherical cloud with a r^{-1} density distribution has a virial mass of

$$M_{\rm VIR} = 190 R \Delta V^2_{\rm FWHM}\, M_\odot \qquad (1)$$

(MacLaren, Richardson, and Wolfendale 1988), where R is the radius of the cloud in parsecs and $\Delta V_{\rm FWHM}$ is the observed full width at half-maximum of the ^{12}CO $J = 1$–0 emission line in kilometers per second. An r^{-1} density distribution was adopted to allow direct comparisons with MS, SG, and Lee, Snell, and Dickman (1990). In general, molecular clouds are not spherical and are not usually completely mapped down to the zero intensity level, so a cloud radius is a rather ambiguous parameter to define. A common approach to estimating the cloud size is to take the square root of the area within some minimum intensity level (see, e.g., Lee, Snell, and Dickman 1990). In this method, however, the cloud size will depend sensitively on the shape of the cloud, the size of the map, and the minimum intensity level, which is often chosen based on the noise in the spectra. To make the cloud sizes more sensitive to the strength of the measured emission and not the quality of our data or the extent of our maps, we have chosen to define the cloud size with the formula

$$R = \frac{\sum_i (I_{^{12}\rm CO})_i [(\alpha_i - \bar{\alpha})^2 + (\delta_i - \bar{\delta})^2]^{1/2}}{\sum_i (I_{^{12}\rm CO})_i}\, d\,, \qquad (2)$$

where $I_{^{12}\rm CO}$ is the integrated ^{12}CO $J = 1$–0 intensity ($\int T_R^* dv$; K km s^{-1}) and d is the distance to the source; (α_i, δ_i) are the coordinates of the ith point, and $(\bar{\alpha}, \bar{\delta})$ is the mean center of the cloud given by

$$\bar{\alpha} = \frac{\sum_i (I_{^{12}\rm CO})_i \alpha_i}{\sum_i (I_{^{12}\rm CO})_i}\,. \qquad (3)$$

Similar weighting schemes were used to estimate $\bar{\delta}$ and the ^{12}CO line width. While these expressions do not give the correct radius for a perfectly uniform, spherical cloud, we believe the limiting factor in our virial mass estimate is the exact form of the virial theorem and not the adopted radius. The radii and line widths for each cloud are summarized in Table 3.

Recently MacLaren, Richardson, and Wolfendale (1988) have suggested that the ^{13}CO $J = 1$–0 line width should be used in place of the ^{12}CO $J = 1$–0 line width in equation (1). They argue that the optically thick ^{12}CO line is likely to be saturation-broadened and therefore overestimate the velocity dispersion and consequently the virial mass estimate, while the narrower, optically thin ^{13}CO line (on average 25% narrower in our sample of clouds) would represent the actual velocity dispersion in the gas. Alternatively, the ^{12}CO and ^{13}CO spectral lines may be created by the superposition of a number of clumps with considerably narrower line widths. Even if saturation broadening increases the ^{12}CO line widths of the individual clumps by 50%, the total increase in the observed line widths of the ensemble of clumps will be at most 10% (see Dickman, Snell, and Schloerb 1986), too small to account for the difference between the ^{12}CO and ^{13}CO line widths. We attribute the broader ^{12}CO lines to the greater extent over which ^{12}CO is detected and presumably a greater number of clumps contributing to the emission. Thus we will quote virial masses using the ^{12}CO line widths in this paper.

A second technique to estimate cloud masses assumes local thermodynamic equilibrium (LTE). As outlined by Dickman (1978), the ^{13}CO column density can be calculated using the ^{12}CO and ^{13}CO observations, and is essentially proportional to the integrated ^{13}CO intensity in the optically thin ^{13}CO limit. The ^{13}CO column density can be converted to the H_2 column density (and hence H_2 mass) by dividing by the

TABLE 3

MILLIMETER OBSERVATIONS

IRAS Source	M_{LTE} ($M_\odot$)	M_{VIR} ($M_\odot$)	$L_{^{12}CO}$ (K km s^{-1} pc^2)	$L_{^{13}CO}$ (K km s^{-1} pc^2)	ΔV_{FWHM} (km s^{-1})	Radius (pc)
00338+6312	2.2×10^3	2.7×10^3	5.1×10^2	1.1×10^2	3.1	1.5
00494+5617	4.3×10^3	4.9×10^3	1.1×10^3	2.1×10^2	3.8	1.9
02593+6016[a]	8.0×10^3	5.8×10^3	2.0×10^3	3.8×10^2	2.9	3.6
03064+5638	2.0×10^2	4.8×10^2	5.6×10	1.0×10	2.2	0.6
04324+5106	2.2×10^4	2.2×10^4	7.4×10^3	1.3×10^3	4.6	5.6
04329+5047	8.9×10^3	1.6×10^4	3.0×10^3	5.5×10^2	3.3	7.7
05100+3723	2.6×10^3	7.3×10^3	6.7×10^2	1.5×10^2	4.2	2.2
05197+3355	8.7×10^2	6.6×10^2	1.9×10^2	3.2×10	2.3	0.7
05274+3345	3.0×10^3	3.6×10^3	6.2×10^2	1.4×10^2	3.2	1.9
05375+3540[b]	3.2×10^4	1.5×10^4	7.6×10^3	1.4×10^3	4.5	3.8
05490+2658	5.2×10^3	3.5×10^3	7.7×10^2	2.2×10^2	3.1	2.0
05553+1631	2.3×10^3	2.4×10^3	5.2×10^2	1.1×10^2	3.0	1.4
06056+2131[c]	9.3×10^3	1.7×10^4	2.2×10^3	4.8×10^2	5.4	3.1
06068+2030	2.9×10^3	4.0×10^3	8.8×10^2	1.5×10^2	3.1	2.2
06073+1249	2.1×10^3	2.4×10^3	1.1×10^3	1.2×10^2	2.2	2.6
06117+1350	9.5×10^3	8.7×10^3	3.0×10^3	4.9×10^2	3.6	3.6
06155+2319	1.7×10^3	2.4×10^3	6.1×10^2	8.9×10	2.8	1.6
06308+0402	1.5×10^3	3.0×10^3	6.5×10^2	7.6×10	3.2	1.6

[a] Derived parameters are for *IRAS* sources 02575+6017 and 02953+6016.
[b] Derived parameters are for *IRAS* sources 05375+3540 and 05377+3548.
[c] Derived parameters are for *IRAS* sources 06056+2131 and 06058+2138.

$^{13}CO/H_2$ abundance, a ratio that has been found to be roughly constant in solar neighborhood dark clouds. The ^{13}CO abundance found in nearby dark clouds is 1.5×10^{-6} (cf. Bachiller and Cernicharo 1986 and Bohlin, Savage, and Drake 1978), the adopted value for this study. To account for the contribution of helium and heavy elements to the cloud mass and to allow for a direct comparison with the virial masses, the H_2 LTE mass has been scaled by 1.36 (Hildebrand 1983) to arrive at the total LTE mass (M_{LTE}).

The masses of the clouds in our sample were calculated using both methods. Only data points with ^{13}CO and ^{12}CO detections 3 σ or better were used in the calculations. The results are tabulated in Table 3 and are plotted in Figure 3. The straight line in Figure 3 is drawn for equal M_{VIR} and M_{LTE} mass estimates. As Figure 3 shows, both mass estimates yield consistent results for cloud masses from a few hundred $M_\odot$ up to a few times 10^4 $M_\odot$.

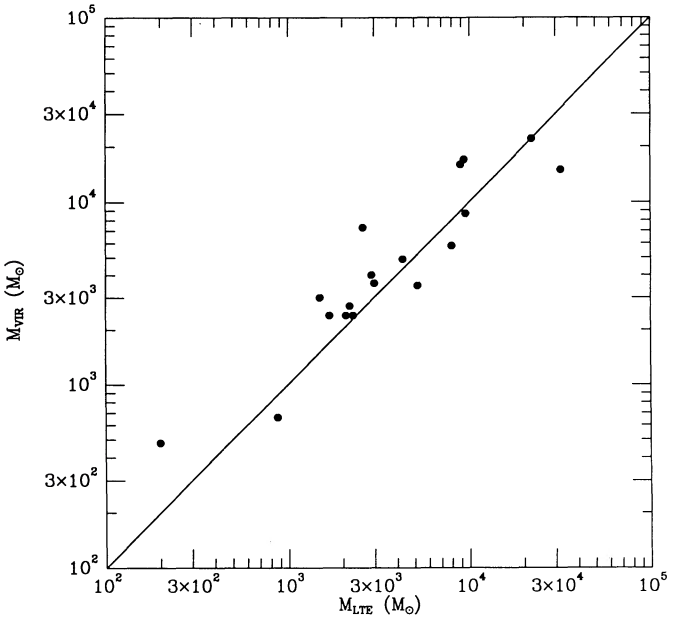

FIG. 3.—Comparison of the virial and LTE mass calculations. The straight line represents equal M_{VIR} and M_{LTE} mass estimates. The average ratio of M_{VIR} to M_{LTE} is 1.3 ± 0.2.

b) ^{12}CO *Luminosity*

Many authors have found the ^{12}CO luminosity, $L_{^{12}CO}$ (K km s^{-1} pc^2), to be strongly correlated with the mass of the cloud despite the fact that ^{12}CO emission is likely to be optically thick and is not expected to trace the molecular gas column density. The ^{12}CO luminosity is found by integrating the ^{12}CO intensity ($I_{^{12}CO}$; K km s^{-1}) over the area of the cloud. We have calculated the ^{13}CO luminosity, $L_{^{13}CO}$, in an analogous fashion and have tabulated the results in Table 3; the average ratio of $L_{^{12}CO}$ to $L_{^{13}CO}$ is 5.6 ± 0.3, where the uncertainty reflects 1 standard deviation of the mean. In Figures 4*a* and 4*b* we plot $L_{^{12}CO}$ versus M_{LTE} and M_{VIR} for the 18 clouds. The solid line in each figure is a nonlinear least-squares fit to the data. We obtained

$$M_{LTE} = (4.70 \pm 0.33) L_{^{12}CO}^{(0.96 \pm 0.06)} M_\odot \quad (4)$$

and

$$M_{VIR} = (16.6 \pm 1.6) L_{^{12}CO}^{(0.81 \pm 0.08)} M_\odot . \quad (5)$$

The slope in equation (5) is in excellent agreement with the value found by Scoville *et al.* (1987), Solomon *et al.* (1987), and Lee, Snell, and Dickman (1990) in their studies of much more massive molecular clouds in the inner Galaxy. The multiplicative factor in equation (4), however, is a factor of 2 or more smaller than their values (see § V).

c) *Far-Infrared Luminosity*

The wealth of far-infrared data from *IRAS* provides an opportunity to estimate the bolometric luminosities of the embedded stars. For ease of comparison with results from MS

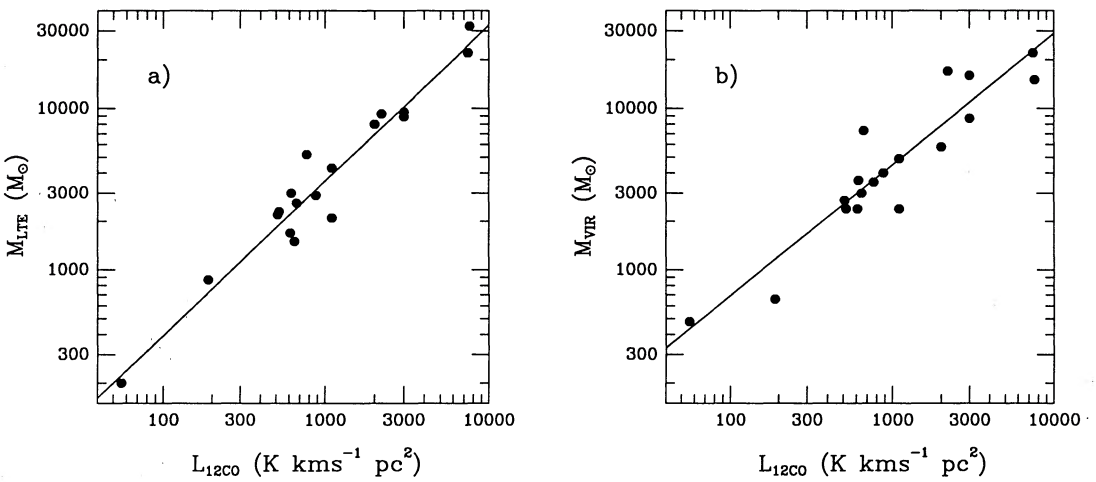

FIG. 4.—(*a*) Plot of LTE mass vs. ^{12}CO luminosity ($L_{^{12}CO}$). The solid line represents a nonlinear least-squares fit to the data; $M_{LTE} = 4.70 L_{^{12}CO}^{0.96}$. (*b*) Plot of M_{VIR} vs. $L_{^{12}CO}$. The solid line represents $M_{VIR} = 16.6 L_{^{12}CO}^{0.81}$.

and SG, we adopt the following formula from Lonsdale *et al.* (1985, Appendix B), which approximates the far-infrared luminosity in the range 1 μm $\leq \lambda \leq$ 500 μm:

$$L_{FIR} = 4\pi d^2[1.26R(1.00 \times 10^{12} S_{100} + 2.58 \times 10^{12} S_{60})] , \quad (6)$$

where d is the distance to the source and S_{60} and S_{100} are the total flux densities at 60 and 100 μm, respectively, obtained from the *IRAS* images within the ^{12}CO mapped regions shown in Figures 1*a*–1*r*. The color correction (R) extrapolates to wavelengths above $\sim$120 μm and below $\sim$40 μm to estimate the energy radiated outside the 60 and 100 μm *IRAS* bands, assuming that all the dust is radiating at the temperature inferred from the 60 and 100 μm fluxes; the color correction is also a function of the emissivity law, which we assume to be λ^{-1}. The factor 1.26 accounts for the flux radiated in the gap between the 60 and 100 μm bands, and 2.58×10^{12} and 1.00×10^{12} Hz are the 60 and 100 μm bandwidths, respectively.

The far-infrared luminosities and colors (ratio of the 60 to the 100 μm integrated flux density) for the 18 molecular clouds are tabulated in Table 4. The luminosities span two orders of magnitude with a general trend of increasing L_{FIR} with cloud mass. The average S_{60}/S_{100} ratio is 0.53 $\pm$ 0.09, corresponding to a dust temperature of 37 $\pm$ 2 for a λ^{-1} emissivity law. All of our sources have emission at 12 and 25 μm that cannot be explained by such a low dust temperature, suggesting the presence of an additional hot dust ($\gtrsim$100 K) component. From the observed flux densities at 12 and 25 μm we calculated the luminosity radiated in these bands and found that L_{FIR}, as defined above, may underestimate the total far-infrared luminosity by as much as 35%, with an average value of around 20%. Since we also have neglected the gap between the 12, 25, and 60 μm bands and any optical or ultraviolet photons that may have escaped from the cloud, L_{FIR} is clearly a lower limit to the actual bolometric luminosity of the embedded stellar objects.

d) Radio Continuum Emission

While the *IRAS* data are useful in estimating the bolometric luminosity, the coarse resolution prevents assigning the far-infrared flux to individual sources. The higher resolution VLA data, however, do provide a means to estimate the spectral type and luminosities of the embedded stars.

Assuming that the H II regions detected are in photoionization equilibrium and optically thin at $\lambda = 6$ cm, we can use the observed integrated flux density to estimate the number of ionizing photons (N_i) emitted by the embedded star. The spectral types of the embedded stars can be estimated from N_i by using the tables in Panagia (1973) and assuming that a single star on the zero-age main sequence is responsible for the ionization. For an optically thin H II region,

$$N_i = 9.0 \times 10^{43} \left(\frac{S_\nu}{\text{mJy}}\right)\left(\frac{d}{\text{kpc}}\right)^2 \times \left(\frac{\nu}{5\ \text{GHz}}\right)^{0.1} \text{photon s}^{-1} , \quad (7)$$

TABLE 4

FAR-INFRARED PROPERTIES

IRAS Source	L_{FIR} ($L_\odot$)	L_{FIR}/M_{LTE} ($L_\odot/M_\odot$)	S_{60}/S_{100}
00338+6312	2.3×10^3	1.1	0.49
00494+5617	2.4×10^4	5.5	0.47
02593+6016[a]	6.2×10^4	7.7	0.51
03064+5638	7.8×10^3	39.2	0.49
04324+5106	5.6×10^4	2.5	0.59
04329+5047	5.7×10^4	6.5	0.47
05100+3723	8.4×10^3	3.2	0.54
05197+3355	9.9×10^3	11.4	0.57
05274+3345	3.8×10^3	1.3	0.44
05375+3540[b]	7.2×10^4	2.2	0.49
05490+2658	1.5×10^4	2.9	0.46
05553+1631	5.9×10^3	2.6	0.68
06056+2131[c]	1.8×10^4	1.9	0.54
06068+2030	1.9×10^4	6.7	0.55
06073+1249	2.5×10^4	11.8	0.78
06117+1350	5.7×10^4	6.0	0.62
06155+2319	8.2×10^3	4.8	0.48
06308+0402	8.2×10^3	5.4	0.43

[a] Derived parameters are for *IRAS* sources 02575+6017 and 02953+6016.

[b] Derived parameters are for *IRAS* sources 05375+3540 and 05377+3548.

[c] Derived parameters are for *IRAS* sources 06056+2131 and 06058+2138.

TABLE 5

PROPERTIES OF THE EMBEDDED STARS

IRAS Source	$\Delta\alpha$	$\Delta\delta$	$N_i/10^{46}$ (s^{-1})	Star[a]
00338+6312	...	...	<0.02	<B2
00494+5617	...	...	<0.08	<B1
02575+6017	0.22	0.03	0.1	B1
02593+6016	0.16	0.08	21	B0
03064+5638	0.25	−0.08	3.7	B0.5
04324+5106	0.22	0.15	64	O9.5
04329+5047	0.25	−0.60	170	O8.5
05100+3723	0.00	0.08	29	B0
05197+3355	0.83	−0.17	1.7	B0.5
	1.41	−0.33	1.2	B0.5
05274+3345	0.33	0.08	0.03	B2
05375+3540	−0.20	0.00	7.2	B0.5
	−0.43	−3.77	1.6	B0.5
05377+3548	−0.08	0.08	0.17	B1
05490+2658	0.16	0.00	0.06	B2
05553+1631	0.00	0.00	0.1	B1
06056+2131	−0.09	0.08	0.03	B2
06058+2138	0.26	−0.42	0.04	B2
06068+2030	0.16	0.08	3.1	B0.5
06073+1249	0.00	0.08	6.3	B0.5
06117+1350	0.34	−0.17	80	O9.5[b]
	4.83	0.50	3.1	B0.5
06155+2319	−0.25	0.50	0.6	B1
06308+0402	0.33	0.00	2.1	B0.5

[a] Spectral type assigned from tables in Panagia 1973 using N_i and assuming the star is on the zero-age main sequence.

[b] The number of ionizing photons includes the emission from the second source listed in Table 2 under 06117+1350. Nearly all of the flux is probably provided by the larger source.

where S_ν is the flux density of the H II region at 5 GHz and d is the distance to the source. In Table 5 we summarize the results from our calculations and estimate the spectral type of the ionizing stars. In most of these regions the observed radio continuum flux is consistent with a single massive star with spectral type of ~B0.

V. DISCUSSION

a) *Mass Determinations*

The CO molecule, although a minor constituent in molecular clouds, has proved to be one of the most important tracers of the molecular phase of the interstellar medium, since the dominant molecular component, H_2, has no permitted rotational transitions. CO spectral lines provide information on cloud kinematics and kinetic temperatures, and are commonly used in estimating molecular cloud masses in LTE and virial analysis, as outlined in § III.

The average ratio of the virial to LTE mass for the 18 clouds in our sample is 1.3 ± 0.2. While the two mass estimates are consistent, several factors contribute to the scatter among them. First, the form of the virial theorem does not take into account the irregular shapes and clumpy nature of molecular clouds and hence is only an approximate solution. Assuming an r^{-2} density distribution, for example, would lower $M_{\rm VIR}$ by a factor of 1.5. Second, the $^{13}CO/H_2$ ratio has an uncertainty of at least 50%. However, in light of a roughly constant ^{13}CO abundance seen in dark clouds, the variation of the true ^{13}CO abundance from cloud to cloud is unlikely to alter systematically $M_{\rm LTE}$. Third, the clouds have not been entirely mapped in ^{12}CO and ^{13}CO, so regardless of the validity of the LTE assumption, the LTE cloud masses should be underestimated. An upper limit to the "unobserved" mass can be obtained by assuming that the ^{13}CO column density at the positions where we have detected only ^{12}CO has a value of the minimum column density computed in the region. We find that on average at least 85% of the total cloud mass has been accounted for in the LTE analysis. Finally, the virial mass estimate is a measure of the entire mass of the cloud, including the cloud mass outside of our mapped regions, so one would expect $M_{\rm VIR}$ to be greater than $M_{\rm LTE}$. Given the uncertainties in all the other parameters, however, it is not clear how large a contribution this effect makes to the differences between $M_{\rm LTE}$ and $M_{\rm VIR}$. Nonetheless, since the LTE and virial mass estimates produced nearly identical results for cloud masses, we believe that the assumptions about the CO abundance and virialization of the clouds that enter into these calculations must be basically correct.

In cases where molecular clouds are not individually resolved, such as in external galaxies, it is not possible to use either technique to derive cloud masses. Thus empirically established relationships between mass and ^{12}CO luminosity are commonly used to estimate molecular gas masses (see Dickman 1988); theoretical justification for such a relationship has been established by Dickman, Snell, and Schloerb (1986), assuming that clouds are gravitationally bound.

Our study can be used to derive the relationship between CO luminosity and cloud mass, and is particularly well suited for this purpose in having a large sample of well-resolved clouds for analysis. Bolstered by the agreement between our two independent mass estimates, we believe that we can accurately determine this relationship. As discussed in an earlier section, a nearly linear relation was found between the LTE mass and ^{12}CO luminosity; the average ratio between these two quantities for the 18 clouds is $3.8 \pm 1.0\ M_\odot\ (\mathrm{K\ km\ s^{-1}})^{-1}\ \mathrm{pc}^{-2}$. A linear relation also provides an adequate fit to the virial mass and CO luminosity data; the average ratio between these two quantities is $4.8 \pm 2.2\ M_\odot\ (\mathrm{K\ km\ s^{-1}})^{-1}\ \mathrm{pc}^{-2}$. However, there is a slight trend for a decreasing ratio with increasing virial mass. Since CO luminosity is used as a mass tracer when individual clouds cannot be resolved, a more consistent way of computing the conversion factor between ^{12}CO luminosity and mass is to use the ensemble average. Using the total ^{12}CO luminosity and total mass, we estimate the conversion factor to be $3.7\ M_\odot\ (\mathrm{K\ km\ s^{-1}})^{-1}\ \mathrm{pc}^{-2}$ and is the same for the LTE and virial mass determinations. Our data demonstrate that over the range of masses in our sample a nearly linear relation exists between molecular cloud mass and ^{12}CO luminosity, and we advocate using a conversion factor of $3.7\ M_\odot\ (\mathrm{K\ km\ s^{-1}})^{-1}\ \mathrm{pc}^{-2}$.

The clouds in our sample are all less than $3 \times 10^4\ M_\odot$ and are considerably smaller than the most massive clouds in the Galaxy. It is unclear, therefore, whether our conversion factor is appropriate for the most massive molecular clouds, which may contribute a large fraction of the total ^{12}CO luminosity in our Galaxy. Scoville *et al.* (1987) and Solomon *et al.* (1987) have used the Massachusetts–Stony Brook Galactic Plane Survey to determine the properties of these massive molecular clouds. The conversion factor derived in these two studies was in the range of $5–8\ M_\odot\ (\mathrm{K\ km\ s^{-1}})^{-1}\ \mathrm{pc}^{-2}$; this is somewhat higher than the value in our sample, although the blending effects for clouds in the inner Galaxy create a large uncertainty in this conversion factor. In another survey, Lee, Snell, and Dickman (1990) have mapped a small region of the first quad-

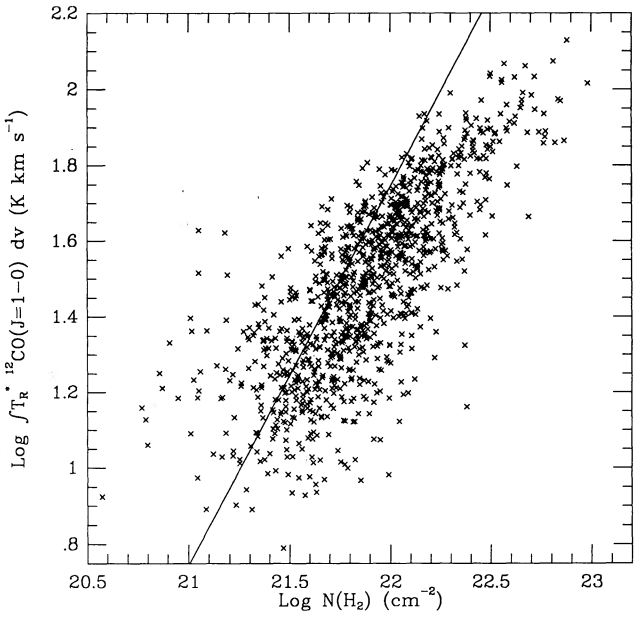

FIG. 5.—Plot of H_2 column density, calculated from the LTE analysis, as a function of the integrated ^{12}CO intensity, $\int T_R^*(^{12}CO)dv$. The solid line represents $N(H_2) = 1.8 \times 10^{20} I_{^{12}CO}$ cm^{-2}, which was calculated from the $L_{^{12}CO}$-M_{LTE} relation.

rant of the Galactic plane in ^{13}CO to derive both virial and LTE masses for a sample of clouds. Their best estimate of the conversion factor is between 3.4 and 6.1 $M_\odot$ (K km s^{-1})$^{-1}$ pc^{-2}. Thus the conversion factor for massive clouds in the inner Galaxy may be slightly larger than for the clouds in our sample. This may indicate a difference between massive and intermediate mass clouds or, alternatively, between inner and outer Galaxy clouds.

The relationship between ^{12}CO luminosity and cloud mass is often represented as an equivalent relationship between ^{12}CO integrated intensity and molecular hydrogen column density, $N(H_2)$. However, the $L_{^{12}CO}$–cloud mass relation represents an average over the face of the cloud and may not reliably give the relation between $I_{^{12}CO}$ and $N(H_2)$ along any particular line of sight. To investigate this possibility, we have plotted in Figure 5 the ^{12}CO integrated intensity versus the molecular hydrogen column density for all lines of sight in the 18 clouds in which both ^{12}CO and ^{13}CO were conclusively detected. A trend clearly exists in the data, but the relationship between $I_{^{12}CO}$ and $N(H_2)$ is not as tight as the one between $L_{^{12}CO}$ and M_{LTE}. Furthermore, Figure 5 also suggests that the H_2 column density may be underestimated at large ^{12}CO integrated intensities using a linear $I_{^{12}CO}$-$N(H_2)$ relation.

b) Star Formation Activity

We have two independent tracers of massive star formation activity within these molecular clouds, the far-infrared and radio continuum luminosities. We first consider the far-infrared luminosity. The far-infrared luminosity ranges from 2×10^3 to 7×10^4 $L_\odot$ for the clouds in our sample, suggesting that all of these clouds are probably sites of O and B star formation. This is not surprising, since the clouds in the sample were selected because of their large far-infrared flux density. A measure of the global rate of massive star formation per unit mass can be obtained from the ratio of far-infrared luminosity to cloud LTE mass (L_{FIR}/M_{LTE}). Since both of these quantities have the same functional dependence on distance, the ratio is distance-independent. We find values for this ratio that range from 1 to 39 $L_\odot/M_\odot$, with an average value of 6.8 $L_\odot/M_\odot$. We can compare this ratio with that derived from infrared bright clouds in the first quadrant of the Galaxy studied by MS and with H II region clouds in the study of SG. These studies typically analyze clouds which are considerably more massive than the clouds in our survey, although both contain clouds with masses of around 10^4 $M_\odot$. MS compute an average ratio of 3.8 $L_\odot/M_\odot$, while SG find a median value of 7.0 $L_\odot/M_\odot$. The similarity of the ratio of far-infrared luminosity to mass between these studies and ours suggests that the average rate of massive star formation per unit molecular mass in massive star-forming regions is the same in both the inner and outer parts of the Galaxy. Furthermore, our average L_{FIR}/M_{LTE} value of 6.8 $L_\odot/M_\odot$ is greater than the average value of 2.8 $L_\odot/M_\odot$ found by SG for all molecular clouds in the plane of the inner Galaxy. Thus the clouds in our sample are forming more stars at a greater rate than an average cloud in the inner Galaxy.

We have plotted in Figure 6 the ratio of far-infrared luminosity to mass as a function of cloud mass for the 18 clouds in our sample and for the infrared bright clouds analyzed by MS and the H II region clouds studied by SG. These investigators used the same data set in analyzing their clouds, and some of the objects in their samples do overlap. We find the range of values of this ratio for our 18 clouds to be similar to that found in the studies of the more massive inner Galaxy clouds, and thus, between 10^2 and 10^7 $M_\odot$, the average and dispersion in the massive star formation rate per unit mass are the same as for inner Galaxy clouds. One cloud, 03064+5638, is particularly noteworthy, since it has a LTE mass of only 200 $M_\odot$ but has a L_{FIR}/M_{LTE} ratio of 39, as large a ratio as the most rapid star-forming clouds in the MS and SG surveys. Yet other

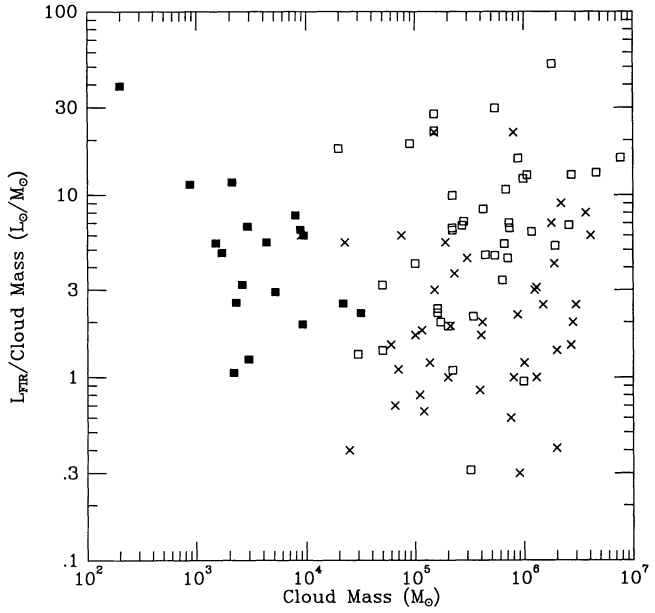

FIG. 6.—Ratio of far-infrared luminosity to cloud mass plotted as a function of the cloud mass. Filled squares are the values for the 18 clouds analyzed in this study, using the LTE mass. Open squares represent the H II region clouds studied by Scoville and Good (1989), and crosses are the infrared bright clouds studied by Mooney and Solomon (1988).

clouds with similar masses, such as Heiles' Cloud 2 and B18, have values of L_{FIR}/M_{LTE} of only 0.3 (Snell, Heyer, and Schloerb 1989) and show no evidence of massive star formation. Thus neither mass nor location in the Galaxy appears to be a factor in determining the rate of massive star formation per cloud mass in molecular clouds.

This suggestion has interesting ramifications for the theory proposed by Scoville, Sanders, and Clemens (1986) that states that the dominant mechanism for OB star formation in the Galaxy is collisions between molecular clouds. Inner Galactic clouds are known to lie in higher cloud density regions than the outer Galactic clouds in our study and are thus expected to undergo more cloud-cloud collisions. Yet we have found no difference in the ratio of far-infrared luminosity to mass in massive star-forming regions in the inner and outer Galaxy. This would seem to imply that if cloud-cloud collisions do indeed induce massive star formation, more collisions do not necessarily enhance the star formation rate per unit mass within a single cloud.

IRAS images of the extended 100 μm emission can be used to probe the environment of the clouds in our survey. Inspection of these images reveals that most of the clouds are part of much larger molecular cloud complexes, assuming that the extended far-infrared emission is a good tracer of the molecular material, as was found by Snell, Heyer, and Schloerb (1989). Thus the clouds we are analyzing are most likely smaller units of the giant molecular cloud complexes studied by MS and SG. Are the ratios of L_{FIR}/M_{LTE} measured for these clumps then a reliable estimate for the entire large molecular cloud complexes? The far-infrared images do show that not only do we increase the mass of the cloud when we encompass more area but we also include more luminous far-infrared sources. For example, the region around 06056+2131/06058+2138/06068+2030 contains a number of equally luminous far-infrared sources, and a larger scale map of this region by Kömpe *et al.* (1989) suggests that most of the mass is associated with these sources with negligible mass distributed between them. Obviously extensive observations are needed to quantify this description and determine whether our calculated luminosity-to-mass ratios apply on a larger scale.

The other measure of the massive star formation activity in these clouds is the integrated flux density at a frequency of 5 GHz. The radio continuum emission was discussed in § IV*d*, where we showed that the ionization in these regions is consistent with a single massive star with a spectral type of ~B0. From the spectral type we can estimate the far-infrared luminosity we would have expected to observe using the tables from Panagia (1973). Within a factor of a few for all of these regions, we found that the stars identified from the radio continuum survey could account for the observed far-infrared luminosity.

It is possible, however, that several unresolved lower luminosity sources may be the ionizing sources as opposed to a single massive star. To get a better indication of the stellar population in these regions, we have obtained near-infrared images at *J*, *H*, and *K* of all 21 sources with 2″ resolution and have found that a cluster of stars is present in most of the molecular clouds (Carpenter, Snell, and Schloerb 1990). It is still quite possible that a single massive star is the dominant ionization source, since the ionization flux decreases steeply as a function of spectral type, to such an extent that even 100 B1 ZAMS stars will not have the ionization flux of a single B0 ZAMS star. We are currently analyzing the near-infrared images to obtain a better census of the stellar population in these molecular clouds.

VI. SUMMARY

We have analyzed the properties of the molecular clouds associated with 21 of the brightest far-infrared sources in the outer Galaxy. The virial and LTE mass estimates for these clouds are in good agreement, which indicates that the assumptions entering into these calculations must be basically correct. In addition, a strong, nearly linear correlation is found between the cloud masses and ^{12}CO luminosities, and we advocate a conversion factor of 3.7 $M_\odot$ (K km s^{-1})$^{-1}$ pc^{-2} between the two quantities. The relation between the H_2 column density and the integrated ^{12}CO intensity along individual lines of sites, however, are not as tightly correlated. The ratio of the far-infrared luminosity to cloud mass for the clouds in our sample has no dependence on cloud mass and has similar values for larger, more massive clouds in the inner Galaxy. This suggests that there is no systematic difference between the rate of massive star formation per unit mass in the inner and outer regions of the Galaxy. We found that a single massive star is likely to be responsible for the ionization in these clouds and could account for most of the observed far-infrared luminosity.

We thank Dave Wonker and Peggy Perley for calibrating the VLA images. This research was carried out under a grant from the NASA Astrophysics Data Program. R. L. S. and F. P. S. also acknowledge partial support from NSF grant AST 88-15406.

REFERENCES

Albert, C. E., Schwartz, P. R., Bowers, P. F., and Rickard, L. J. 1986, *A.J.*, **92**, 75.
Bachiller, R., and Cernicharo, J. 1986, *Astr. Ap.*, **166**, 283.
Bennett, C. L., Lawrence, C. R., Garcia-Barreto, J. A., Hewitt, J. N., and Burke, B. F. 1983, *Nature*, **301**, 686.
Blitz, L., Fich, M., and Stark, A. A. 1982, *Ap. J. Suppl.*, **49**, 183.
Bohlin, R. C., Savage, B. D., and Drake, J. F. 1978, *Ap. J.*, **224**, 132.
Carpenter, J. M., Snell, R. L., and Schloerb, F. P. 1990, in preparation.
Chavarría-K., C., de Lara, E., and Hasse, I. 1987, *Astr. Ap.*, **171**, 216.
Chavarría-K., C., Leitherer, C., de Lara, E., Sánchez, O., and Zickgraf, F.-J. 1989, *Astr. Ap.*, **215**, 51.
Chopinet, M., Deharveng-Baudel, L., and Lortet-Zuckermann, M. C. 1974, *Astr. Ap.*, **30**, 233.
Cohen, M. 1980, *A.J.*, **85**, 29.
Cohen, M., Jones, B. F., and Walker, H. J. 1989, *Ap. J.*, **341**, 908.
Cox, P., Deharveng, L., and Caplan, J. 1987, *Astr. Ap.*, **171**, 277.
Dickman, R. L. 1978, *Ap. J. Suppl.*, **37**, 407.
———. 1988, in *Molecular Clouds in the Milky Way and External Galaxies*, ed. R. L. Dickman, R. L. Snell, and J. S. Young (Dordrecht: Reidel), p. 55.
Dickman, R. L., Snell, R. L., and Schloerb, F. P. 1986, *Ap. J.*, **309**, 326.
Elmegreen, B. G., and Lada, C. J. 1977, *Ap. J.*, **214**, 725.
Elmegreen, B. G., and Lada, C. J. 1978, *Ap. J.*, **219**, 467.
Evans, N. J., II, and Blair, G. N. 1981, *Ap. J.*, **246**, 394.
Felli, M., Habing, H. J., and Israël, F. P. 1977, *Astr. Ap.*, **59**, 43.
Felli, M., Hjellming, R. M., and Cesaroni, R. 1987, *Astr. Ap.*, **182**, 313.
Frogel, J. A., and Persson, S. E. 1973, *Ap. J.*, **186**, 207.
Garnier, R., and Lortet-Zuckermann, M. C. 1971, *Astr. Ap.*, **14**, 408.
Gebel, W. L. 1968, *Ap. J.*, **153**, 743.
Grasdalen, G. L., and Carrasco, L. 1975, *Astr. Ap.*, **43**, 259.
Heydari-Malayeri, M., Testor, G., Baudry, A., Lafon, G., and de la Noë, J. 1982, *Astr. Ap.*, **113**, 118.
Hildebrand, R. H. 1983, *Quart. J.R.A.S.*, **24**, 267.
IRAS Point Source Catalog. 1985, Joint *IRAS* Science Working Group (Washington, DC: GPO).
Israël, F. P. 1977, *Astr. Ap.*, **60**, 233.
Israel, F. P., and Felli, M. 1978, *Astr. Ap.*, **63**, 325.
Kazés, I., Le Squéren, A. M., and Gadéa, F. 1975, *Astr. Ap.*, **42**, 9.
Kömpe, C., Joncas, G., Baudry, A., and Wouterloot, J. G. A. 1989, *Astr. Ap.*, **221**, 295.
Kutner, M. L., and Ulich, B. L. 1981, *Ap. J.*, **250**, 341.
Lada, C. J. 1985, *Ann. Rev. Astr. Ap.*, **23**, 267.
Lada, C. J., and Wooden, D. 1979, *Ap. J.*, **232**, 158.

Lee, Y., Snell, R. L., and Dickman, R. L. 1990, *Ap. J.*, **355**, 536.
Lo, K. Y., and Burke, B. F. 1973, *Astr. Ap.*, **26**, 487.
Lonsdale, C. J., Helou, G., Good, J. C., and Rice, W. L. 1985, *Catalogued Galaxies and Quasars Observed in the IRAS Survey* (Washington, DC: GPO).
Loren, R. B., and Wootten, H. A. 1978, *Ap. J. (Letters)*, **225**, L81.
Lucas, R., and Encrenaz, P. J. 1975, *Astr. Ap.*, **41**, 233.
MacLaren, I., Richardson, K. M., and Wolfendale, A. W. 1988, *Ap. J.*, **333**, 821.
Mampaso, A., Phillips, J. P., Vílchez, J. M., Pismis, P., and Riera, A. 1989, *Astr. Ap.*, **220**, 235.
Moffat, A. F. J., FitzGerald, M. P., and Jackson, P. D. 1979, *Astr. Ap. Suppl.*, **38**, 197.
Mooney, T. J., and Solomon, P. M. 1988, *Ap. J. (Letters)*, **334**, L51 (MS).
Neckel, T., and Staude, H. J. 1984, *Astr. Ap.*, **131**, 200.
Panagia, N. 1973, *A.J.*, **78**, 929.
Persi, P., Ferrari-Toniolo, M., Shivanandan, K., and Spinoglio, L. 1987, *Astr. Ap. Suppl.*, **70**, 437.
Pottasch, S. 1956, *Bull. Astr. Inst. Netherlands*, **13**, 77.
Sanders, D. B., Clemens, D. P., Scoville, N. Z., and Solomon, P. M. 1986, *Ap. J. Suppl.*, **60**, 1.
Scoville, N. Z., and Good, J. C. 1989, *Ap. J.*, **339**, 149 (SG).
Scoville, N. Z., Sanders, D. B., and Clemens, D. P. 1986, *Ap. J. (Letters)*, **310**, L77.
Scoville, N. Z., Yun, M. S., Clemens, D. P., Sanders, D. B., and Waller, W. H. 1987, *Ap. J. Suppl.*, **63**, 821.
Sharpless, S. 1959, *Ap. J.*, **4**, 257.
Snell, R. L., Dickman, R. L., and Huang, Y.-L. 1990, *Ap. J.*, **352**, 139.
Snell, R. L., Heyer, M. H., and Schloerb, F. P. 1989, *Ap. J.*, **337**, 739.
Snell, R. L., Huang, Y.-L., Dickman, R. L., and Claussen, M. J. 1988, *Ap. J.*, **325**, 853.
Solomon, P. M., Rivolo, A. R., Barrett, J., and Yahil, A. 1987, *Ap. J.*, **319**, 730.
Thronson, H. A., Jr., Thompson, R. I., Harvey, P. M., Rickard, L. J. and Tokunaga, A. T. 1980, *Ap. J.*, **242**, 609.
Turner, B. E. 1971, *Ap. Letters*, **8**, 73.
Turner, K. C., and Terzian, Y. 1985, *A.J.*, **90**, 59.
Wynn-Williams, C. G., Becklin, E. E., and Neugebauer, G. 1974, *Ap. J.*, **187**, 473.
Zeilik, M., II. 1976, *Astr. Ap.*, **46**, 319.

JOHN M. CARPENTER, F. PETER SCHLOERB, and RONALD L. SNELL: Five College Radio Astronomy Observatory, Department of Physics and Astronomy, University of Massachusetts, Amherst, MA 01003